REVIEW

An Invited Review for the Special 20th Anniversary Issue of MRMS

New Insights into MR Safety for Implantable Medical Devices

Kagayaki Kuroda[1*] and Satoshi Yatsushiro[1,2]

Over the last two decades, the status of MR safety has dramatically changed. In particular, ever since the MR-conditional cardiac device was approved by the Food and Drug Administration (FDA) in 2008 and by the Pharmaceuticals and Medical Devices Agency (PMDA) in 2012, the safety of patients with an implantable medical device (IMD) has been one of the most important issues in terms of MR use. In conjunction with the regulatory approvals for various IMDs, standards, technical specifications, and guidelines have also been rapidly created and developed. Many invaluable papers investigating and reviewing the history and status of MR use in the presence of IMDs already exist. As such, this review paper seeks to bridge the gap between clinical practice and the information that is obtained by standard-based tests and provided by an IMD's package insert or instructions for use. Interpretation of the gradient of the magnetic flux density intensity of the static magnetic field with respect to the magnetic displacement force is discussed, along with the physical background of RF field. The relationship between specific absorption rate (SAR) and B_{1+RMS}, and their effects on image quality are described. In addition, insofar as providing new directions for future research and practice, the feasibility of safety test methods for RF-induced heating of IMDs using MR thermometry, evaluation of tissue heat damage, and challenges in cardiac IMDs will be discussed.

Keywords: B_{1+RMS}, heating, imaging condition, implantable medical device, specific absorption rate

Introduction

Until the early 1990s, the most feared danger associated with MRI was the projectile effect resulting from a static magnetic field. MRI has been regarded as a non-invasive imaging method insofar, as it does not expose patients to ionizing radiation. However, the researchers who developed the MR scanners in the early 1980s questioned whether the static magnetic field, oscillating gradient magnetic field, and RF magnetic field used in MR scanners had significant effects on the human body. In Japan, Tateno, Kamei et al. established the Committee on Recent Knowledge of Magnetic Field Effects and Safety in NMR Images at the Nuclear

Magnetic Resonance Medicine Study Group, and initiated an industry-academia collaborative study on the safety of the three kinds of magnetic fields in 1982.[1] In 1983, Nakatsugawa Municipal Hospital, which is the first clinical facility that introduced an MR system in Japan, published a survey report on the effects of MR examination on humans at 0.04 Tesla.[2] In 1984, the results of a "Questionnaire survey on changes in the physical condition and morbidity of researchers using high magnetic field devices" were published by the Effects and Safety of Magnetic Fields Committee in Japan.[3]

Since safety standards became indispensable during the spread of clinical MR scanners, the Food and Drug Administration (FDA) in the United States established an MR safety guideline in 1982.[4] The FDA's guideline was established by the International Electrotechnical Commission (IEC) as the medical electrical equipment standard IEC60601-2-33.[5] The revision of the FDA's guideline in 1988 set limits for static magnetic field strength, magnetic field change rate, RF heating, and noise level, eliminating the need for premarket authorization (PMA) or premarket notification 510(k) for MR scanners of 2 T or less.[6] In parallel, the National Electrical Manufacturers Association (NEMA) established several important procedures including those for measuring time-varying gradient fields (dB/dt)[7] and specific absorption rate

[1]Department of Human and Information Sciences, School of Information Science and Technology, Tokai University, Hiratsuka, Kanagawa, Japan
[2]Biosim Laboratory, Bioview, Inc., Tokyo, Japan

*Corresponding author: Department of Human and Information Sciences, School of Information Science and Technology, Tokai University, 4-1-1 Kitakaname, Hiratsuka, Kanagawa 259-1292, Japan. Phone: +81-463-63-4178 (Laboratory), +81-463-63-4211 (Office), E-mail: kagayaki@keyaki.cc.u-tokai.ac.jp

(SAR).[8] At that time, The Japan Radiological Equipment Manufacturers Association (currently known as the Japan Medical Imaging and Radiological Systems Industries Association [JIRA]) also standardized the "Guidelines for attraction of magnetic materials by magnetic fields".[1] The history of MR safety in these early days is detailed further across many sources.[9–12]

In 2010, the IEC standards for MR scanner safety were revised,[13] with the latest amendment having been published in 2015.[14] This standard systematically describes the limit values for the static magnetic field, gradient field, and RF field based on the concept of operation modes—that is normal mode, first-order controlled operation mode, and second-order controlled operation mode. When examining a human body, all outputs of the magnetic fields are controlled to be within the allowable range. Figure 1 shows an overview of the elements and technologies to ensure patient safety and comfort in MR examination.[1]

In parallel to the development of MR technology, implantable medical devices (IMD) have also been developed with the trend of minimally invasive treatment for various diseases. Nowadays, there are many opportunities for patients with devices in their body to undergo MR examination. With the spread of high field scanners and the increasing importance of MR examinations, the demand to inspect a patient with an IMD has rapidly increased. The human body is diamagnetic and does not feel magnetic displacement force or torque due to the static magnetic field and/or spatial field gradient. Indeed, a person may feel nerve stimulation including vertigo, nausea and dysgeusia due to eddy currents generated in the body when the patient moves in the static magnetic field,[15–18] vibration due to gradient magnetic field switching, or increase in body temperature due to the RF magnetic field. However, these phenomena do not reach a dangerous level so long as the clinical scanners are set to the appropriate imaging condition by IEC standard.[14] This makes it difficult to perceive the interaction between the magnetic fields and IMDs in a patient's body. To predict the interaction of the magnetic fields with IMDs containing magnetic or conductive materials, it is necessary to know the physics behind them.[19] Armed with the knowledge of safety standards that have been precisely constructed based on such physics, it is then possible to decipher the MR-conditional information described in the package insert of an IMD. Moreover, there are already several excellent reviews associated with the development and progress of standards. For example, the situation in the dawn of MR safety for IMDs is described by Davis.[20] The history of IMD-related standards is well covered by Woods.[21] There are also several papers describing RF heating of various passive IMDs (PIMD).[22,23] For the MR conditionality of active IMD (AIMD), including cardiac devices like pacemakers (PM), implantable cardioverter defibrillators (ICD), and cardiac resynchronization therapy defibrillators (CRT-D), a large number of review papers have been published.[23–34]

Thus, this paper will focus on carefully selected topics to bridge the gap between clinical practice and the information obtained by standard-based tests and provided by an IMD's package insert or manual. First, we will conduct a brief review of MR safety for IMDs and clarify the current issues with which we are facing. Second, as issues are common to both active and passive implants, we will examine the physical background of the displacement force and RF heat generation, which are sometimes difficult to understand in the form supplied in standards. Third, the gap between the console-displayed SAR/$B_{1+\text{RMS}}$ of the device and the measured SAR will be elucidated. Furthermore, to clarify how the RF power condition has a practical effect on clinical output, the conditions of SAR and $B_{1+\text{RMS}}$ in the routine examination conditions for various body parts will be discussed. In terms of suggesting future directions for maintaining MR safety for IMDs, the feasibility of RF heating assessment based on MR thermometry will be discussed. Moreover, New MR safety issues for cardiac AIMD will be discussed.

Brief Historical Review of MR Safety for IMDs

In response to the rapid and widespread employment of clinical MR examinations across the world, the Center for Devices and Radiological Health (CDRH) of the FDA started to prepare appropriate standards to address the safety of using MR in the presence of implantable and other medical devices.[21] It is known that the CDRH requested that the American Society for Testing and Materials (ASTM) develop test methods and guidance for IMDs to maintain MR safety. Based on the request, ASTM formed a task group called F04.15.11 that was responsible for developing the test methods for evaluating MR safety for passive IMDs. Here, passive means that the device does not have an electrical source. After the first standard for magnetically induced force, F2052, was published in 2000,[35] the task group published and revised the standards for magnetically induced force, F2052; torque, F2213; and RF field-induced heating, F2182. The standards for image artifact, F2119, as well as marking practice, F2503, for MR conditionality were also developed and revised. Note that only the latest versions, F2052-15,[36] F2213-17,[37] F2182-19e2,[38] F2119-07 (reapproved in 2013),[39] and F2503-20,[40] are the active standards that currently apply. The version history of these standards is fully viewable at the ASTM website.[41]

In Japan, the 2003 Ministry of Health, Labor and Welfare notification includes the following description about IMD effects on MRI: "Evaluate the effect of implanted stents on heat generation, artifacts (magnetic field interference), etc. during MRI examination." This is the ministry's first mention of MR safety for IMDs in Japan. In a 2008 notice, the ASTM standard was first referred to as a valid test method by the ministry, described as "the test of hanging a clip with a thin wire in a magnetic field environment will be conducted
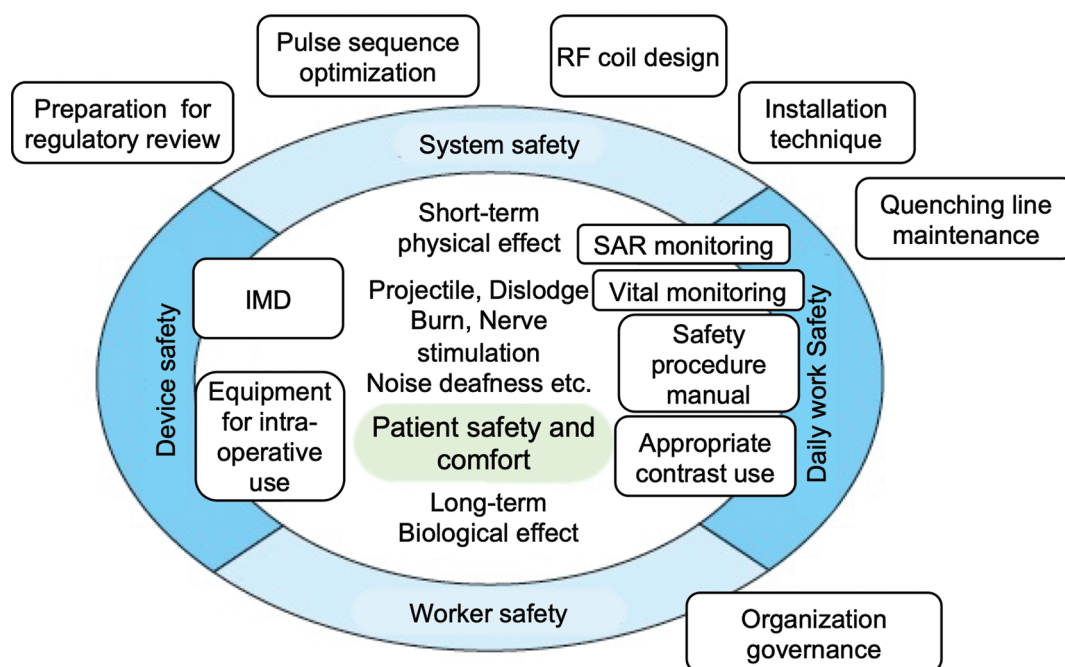
Fig. 1 MR Safety elements and technologies to ensure patient safety and comfort. The viewpoints of MR safety are roughly divided into the safety of MR system, safety for IMDs and intraoperative equipment around MR system, safety management in daily clinical practice, and the safety of MR workers. IMD, implantable medical devices. (Translated and modified from reference #1)

based on the ASTM F2052 test method." In response to these notifications, the momentum for MR safety assessment for IMDs has rapidly increased in Japan.

One of the greatest advances in improving upon MR safety for IMDs was the approval of the MR-conditional cardiac pacemaker by the FDA in 2008 and Pharmaceuticals and Medical Device Agency (PMDA) in 2012. Prior to this, cardiac pacemakers categorized as active, that is, IMDs with an electrical power source, had been basically contraindicated for MR examination. MR safety for AIMDs was not completely covered by the existing ASTM standard, however. When the cardiac device was approved as an MR-conditional device, MR safety assessment technology for AIMDs made great progress and led to joint work carried out by the International Organization for Standardization (ISO) and the IEC. In June 2014, this work yielded the technical specification ISO TS10974, "Assessment of the safety of magnetic resonance imaging for patients with an active implantable medical device".[42] The ASTM standards are fully referenced in this ISO specification. Furthermore, the second edition of these ISO specifications was published in 2018.[43] In this edition, 12 types of hazards that can be caused by the 3 kinds of MR magnetic fields were identified, as shown in Fig. 2. Currently, this technical specification is an evaluation guideline to be applied to all AIMDs, including pacemaker (PM), implantable cardiac defibrillator (ICD), CRT-D and cardiac resynchronization therapy-pacemaker (CRT-P), leadless pacemaker, deep brain stimulator (DBS), spinal code stimulator (SCS), vagal

nerve stimulator (VNS), artificial auditory devices, and others. In the naming convention of ISO, TS stands for technical specification, and normally, the third revision of TS will promote the technical specification as an international standard, IS. In addition to such a horizontal standard, where necessary, individual classes of AIMDs (e.g. PM) have their own vertical standard (e.g. PC76 from Association for the Advancement of Medical Instrumentation [AAMI]).

The imaging conditions for these AIMDs improved rapidly after the publication of TS-10974 with the continuous effort of the joint working group (JWG) of ISO/TC 150/SC 6/JWG2[44] and IEC/SC 62B/JWG 1.[45] The conditions are specified in a device's instructions for use (IFU) or package insert. For cardiac devices used in Japanese hospitals, the conditions for safe MR imaging can also be researched in the Japan Arrhythmia Device Industry Association (JADIA) database. In contrast to the database provided by individual manufacturers, the JADIA is unique in that users can look up MR safety information for different manufactures in a cross-sectional manner. In addition, the MR conditionality lists for cardiac devices, cochlear implants, and vagal nerve stimulators are provided on the homepage of the Japanese Society for Magnetic Resonance in Medicine (JSMRM).[46]

On the other hand, insufficient information, that is non-labeling or MR conditional labels of poor quality, provided in the package inserts for passive IMDs often poses problems at clinical sites. There are several databases containing MR safety information.[47–49] A comprehensive MR safety database
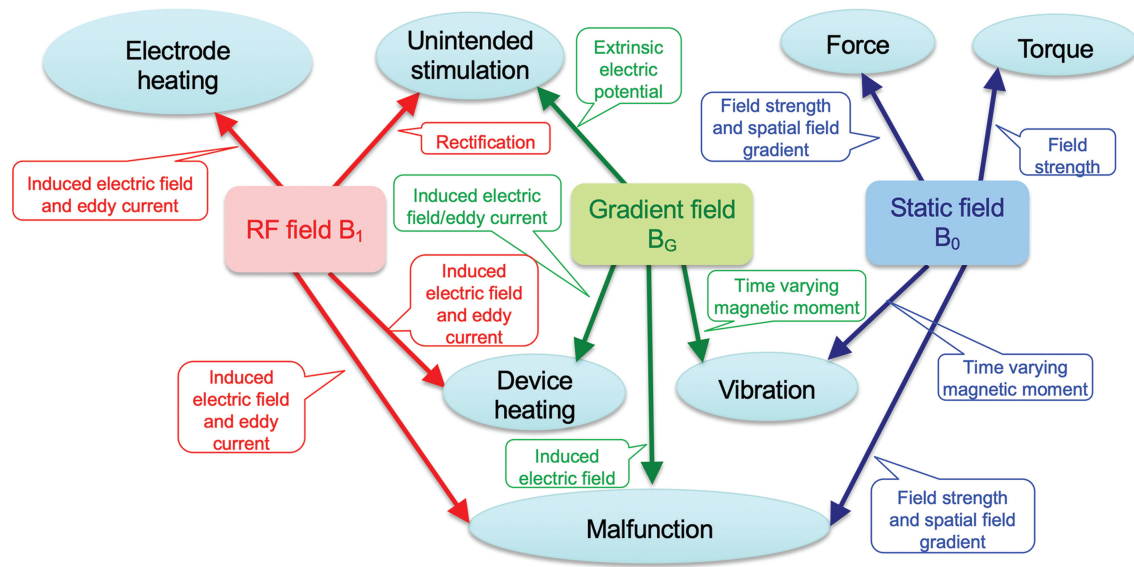
Fig. 2 Relationships between the magnetic fields used in the MR scanner (Static, gradient, and RF) and hazards for the implantable medical device. (Modified from reference #43)

provided free of charge by a Japanese company revealed that MR safety information is provided in package inserts for less than half of all existing IMD products at the time of writing, and even when provided, it is sometimes extremely insufficient. In 2014, Japan's Ministry of Health, Labor, and Welfare (MHLW) conducted a research project entitled "Research on evaluation of the effects of MR imaging on medical devices and how safety information should be provided." In the final report of this project, recommendations and guidance for labeling and describing MR safety information were provided. Furthermore, in response to this report, a document entitled "Measures for MR safety for IMD" was issued in August 2019. This document required that, 3 years after its publication, manufacturers of metal-containing IMDs (including temporally indwelled devices) attach the results of safety evaluations for new medical devices, class IV medical devices, and class III active medical devices when applying for new manufacturing and marketing approval. Note that the classification system described here is the Japanese system. The correspondence of the classification systems in different country area is summarized elsewhere.[50] Existing approved products are also required to be accompanied by MR safety information within 3 years of the document's release for Class IV and Class III equipment and within 5 years for Class II and I equipment. As a result of these requirements, the inclusion of MR safety descriptions in package inserts is currently advancing in Japan.

Tips for Understanding MR Conditionality

In this section, important tips for understanding the physical meanings of MR conditionality are described. Unlike the detailed testing procedures described in standards and textbooks, only main topics are described here.

Magnetically induced displacement force

Attraction due to magnetic displacement force on a magnetic material has been the most common hazard associated with MR[51] and has caused serious accidents including a recent fatal one.[52] The magnetically induced displacement force acting on the subject can be measured by taking the tangent of the deflection angle with respect to gravity while suspended from a string. The spatial position where this force is maximized is at the position where the gradient of the magnitude of the magnetic flux density of the static magnetic field (spatial field gradient for short) $|\nabla B_0|^{*1*2}$ is the maximum, when the ferromagnetic material is magnetically saturated. For example, in iron or steel, the saturation will occur when the applied magnetic field intensity is 3000–5000 [A/m53]), which is corresponding to 3.8–6.3 (mT) in the void. Since this value is easily attainable near the gantry of clinical scanners, the displacement force is determined only by the spatial field gradient. In the case of a diamagnetic, paramagnetic, or unsaturated ferromagnetic material, the force is maximized at the position where the product of B_0 and $|\nabla B_0|$ is the maximum. In a 1.5-T and 3-T superconducting and horizontal magnet, the largest value of the product is near the entrance of the gantry, as shown in Fig. 3. Although in the previous ASTM F2503-06 standard, such a position had to be found to measure the maximum displacement force, it is difficult to accurately find the position. Therefore, in the current standard F2503-15,[36] the maximum value of the allowable static magnetic field strength gradient is obtained by

---

*1 ∇ is called nabla and is a differential operator (vector) that expresses the spatial gradient. The description ∇B_0 shows the spatial gradient of the magnitude (scalar) of the magnetic flux density of the static magnetic field.
*2 Note that the bold italic font $\boldsymbol{B_0}$ represents a vector, while the fine and italic font B_0 represents a scalar, and thus the magnitude of a vector $\boldsymbol{B_0}$. Such electromagnetic convention is applied throughout the entire text.
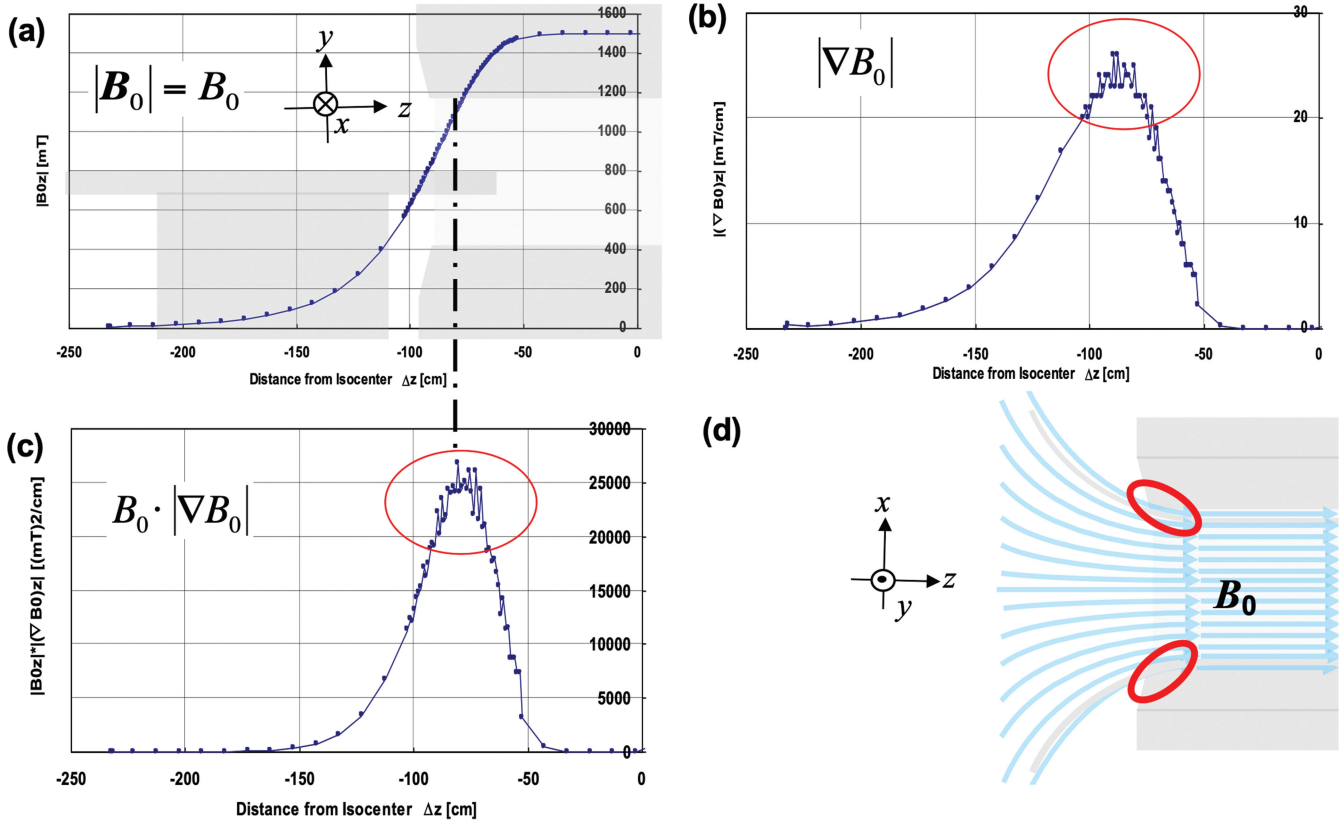
Fig. 3 Typical example of distribution of intensity of magnetic flux density (**a**) and its gradient (**b**) measured along the z-axis of a horizontal 1.5-T scanner. The product of the flux density intensity and the gradient is shown in (**c**). Thin red ellipses show the peak regions of the spatial field gradient or the product, where the magnetically induced displacement force to an IMD becomes strongest on the z-axis. Note that the measurements were made only on the z-axis. The position where the strongest displacement force acts on an IMD is located near the edge of the gantry as indicated by thick red ellipses on the schematically illustrated coronal view of the gantry (**d**).

measuring on the z-axis and giving the target static magnetic field strength and the deflection angle. That is, when the deflection angle is α_L [deg] at a position where the magnitude of the magnetic flux density is B_{0L} (T), and the absolute value of the gradient of the magnitude of the magnetic flux density is $|\nabla B_0|_L$ (T/m), we may assume certain target values of the deflection angle α_C (deg) and the magnitude of the magnetic flux density B_{0C} (T). Then, the allowable gradient $|\nabla B_0|_C$ (T/m) can be calculated using the following equation:

$$|\nabla B_0|_C = |\nabla B_0|_L \cdot \frac{B_{0L}}{B_{0L}} \cdot \frac{\tan \alpha_C}{\tan \alpha_L} \qquad (1).$$

If this value is greater than the maximum gradient of the magnetic flux density intensity of the static magnetic field in the MRI system used for inspection, the magnetic displacement force is at an allowable level. For example, suppose that the measured value of the deflection angle for a certain sample α_L is 10 degrees, the magnetic flux density intensity of the static magnetic field B_{0L} is 1.1T and its gradient is

$|\nabla B_{0L}|$ is 25T/m, as shown in Fig. 3. If the deflection angle α_C is assumed to be 45 degrees aiming for a magnetic displacement force equal to or less than gravity, and the target magnetic flux density B_{0C} is 1.5T, the allowable gradient $|\nabla B_0|_C$ becomes 104 T/m. Since the typical maximum value of the gradient of the magnitude of the magnetic flux density of the static magnetic field in a common clinical 1.5T MRI device is 19 T/m,[36] the allowable value well exceeds this. In this case, the sample should be safe in terms of displacement force. As a side note, the typical maximum gradient in the 3T is 17 T/m.[36] It should be noted that a weak static magnetic field does not necessarily mean that the gradient is small.

The Physics behind RF Heating

The RF magnetic field (64 MHz at 1.5T and 128 MHz at 3T) generated by a whole-body coil rotates in the *xy* (axial) plane shown in Fig. 4a. This magnetic field induces an electric field in the subject in the form of swirling in the *zx* (coronal) plane as shown in Fig. 4b, which induces an electric current

generating heat with the resistance of phantom material or tissue. When a metal rod is placed at the lateral region to be parallel to this electric field, a heat distribution occurs as shown in Fig. 4b. If a bare conductive rod is in place, SAR distributes over the length of the rod as shown in the bottom right of the figure with a color scale bar. If the metal rod is insulated leaving both ends exposed, the SAR will be concentrated on the exposed parts at both ends. When the **E**-field is tangential to the conductor, heating potential is highest. In this way, the heat generated by metal objects changes significantly depending on the angle with respect to the **E**-field direction as depicted in the figure with different angles.

There are two basic mechanisms for such heat generation. One is the current concentration and the other is the induction. As shown in Fig. 5a, the current distributed at a density around the metal rod concentrates into the exposed end of the rod because the conductivity of the metal is higher than that of the surrounding tissue. After flowing through the conductor, the current flows out and spreads rapidly, when it reaches the opposite exposed end. For example, when the radius R_i of the metal rod is 1 mm and the length l is 50 mm, the current density in the hemispherical region, where the radius R_o of the exposed end is 5 mm, is calculated as about 30 times the surrounding current density.[54] Since SAR is determined by the square of the current density, it reaches about 900 times the surrounding current density.

On the other hand, even if the metal rod is insulated leaving only one side exposed, heat is generated at the exposed end. As shown in Fig. 5b, the tangential component $E_{tan}(\tau)$ of the surrounding electric field couples with a small segment $\Delta\tau$ of the conductor at a distance τ from the tip inducing electric current in the conductor. Such an electric current flows out of the exposed end, causing electric field $\Delta E_S(\tau, P)$ at a spatial point P near the tip. The total electric field will be the sum of the field caused by the tangential component at every segment of the lead. Such a total electric field causes high SAR in the tissue around the tip.[55]

In addition, when the length of a conductive material is close to the half wavelength of the electromagnetic field, there will be a standing wave. It is well known that the SAR around a bare or insulated wire is maximized when the length of the wire is half the length of the ambient electromagnetic field because the standing wave is generated on the wire, making the electric charge density at both ends of the wire highest.[19] This mechanism is analogous with a dipole antenna whose electric length is taken to be the same with the half wavelength. The wavelength λ is determined by the following equation:

$$\lambda = \frac{1}{\sqrt{\varepsilon_r \mu_r}} \cdot \frac{C_0}{f} \qquad (2),$$

where C_0 is speed of electromagnet wave propagation in vacuum (= 3.0×10^8 m/s), f is frequency, ε_r is relative permittivity, and μ_r is relative permeability. The wavelength in the phantom material or tissue is in inverse proportion to the square root of the relative permittivity of a media, assuming that the permeability is equivalent to that in vacuum. As ε_r is around 80 in ASTM Phantom or equivalent in a human body, the wavelength is about 1/9 of that in vacuum. The length is around 52 cm at 1.5T (64 MHz) and 26 cm at 3T. Thus, the half of wavelength of 26 cm at 1.5T or 13 cm at 3T can be the resonant length for inducing the standing wave. With such a standing wave formation, the dissipation of the electrical power at the tip of a conductor becomes larger than in the instance without a standing wave.[56] The extent of the increase is based on the difference in the impedance between the tissue and the IMD material. When the impedance of the IMD material is more conductive than the surrounding tissue, the concentration of the electric current, and thus the standing wave amplitude, becomes larger, resulting in higher SAR concentration induced by electric charge dissipation at the boundary between the material and tissue.

These are the basic reasons why SAR is concentrated at the tip of the lead wire of the cardiac device.[57]

However, it is not easy to predict the contribution to RF-induced heat from each of the above-mentioned mechanisms. Thus, simple numerical simulations of a lead's heat generation properties were conducted to elucidate this issue, as follows.[58] An insulated lead with either both ends or one end of the core wire left bare was modeled as depicted in Fig. 6a. The core wire was assumed to be a perfect conductor (infinite conductivity with no resistance) with a diameter of 1.6 mm. The length of the bare part(s) was 20 mm. The other part of the wire was covered with a dielectric material with a thickness of 0.4 mm. This lead model was placed in the lateral side of an ASTM phantom material, depicted by a black bar in Fig. 6b. The phantom was then placed in an 8-leg lowpass birdcage type body coil so that the gravity center of the trunk was aligned at the center of the RF body coil. The overall length of the conductive wire and the relative permittivity of the dielectric material were systematically changed to observe changes in SAR based on those variables. The simulation was performed using a finite difference time domain (FDTD) method on commercial software (Sim4Life, Zurich Med Tech AG, Zurich, Switzerland). The RF magnetic field was created by a continuous sinusoidal electric current source on each of the birdcage legs with 1-A amplitude.

The resultant maximum local SARs for both-end and one-end cases at 3T are shown in Fig. 6c and 6d. In the both-end exposed case (c), changes in length and permittivity changed SAR modestly compared with the one-end exposed case (d) because the contribution of the electric current inflow and outflow at the open ends was dominant, and thus less affected by the property of the insulation material. A vague peak was recognized at around $l = 125 \sim 130$ mm, which corresponds to half of wavelength λ of the 128 MHz electromagnetic field in the phantom material,

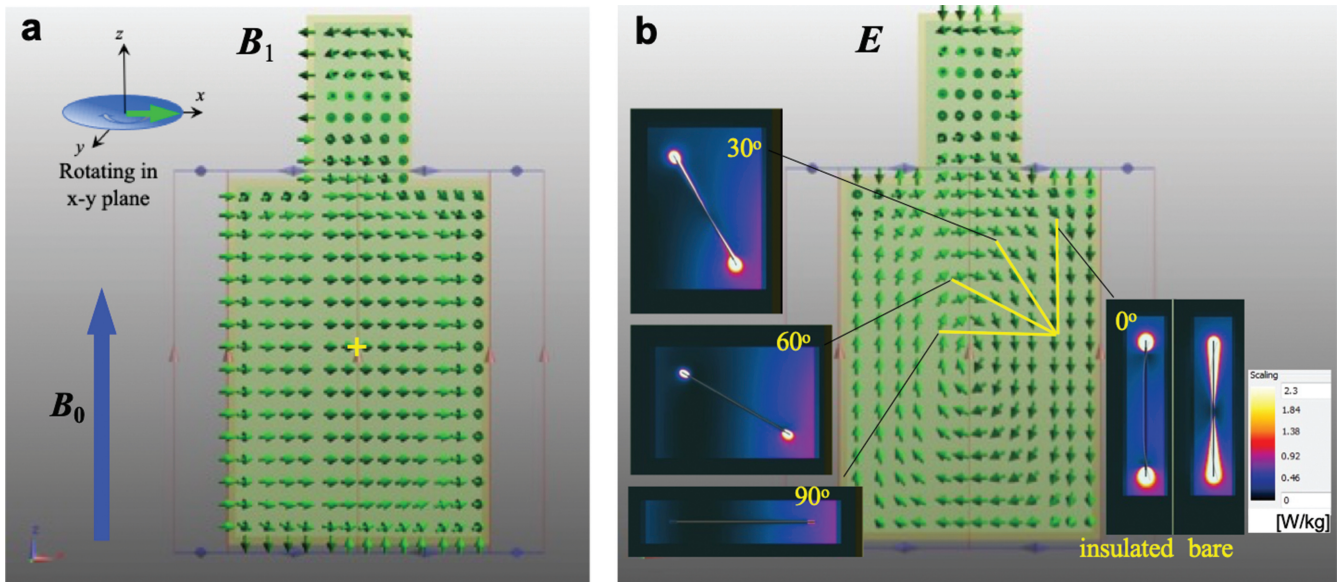**Fig. 4** Coronal view of the behavior of RF magnetic field, B_1 (**a**), and electric field, E (**b**) numerically simulated on the z-x ($y = 0$) plane of the ASTM phantom in a horizontal 1.5-T scanner. The static magnetic field was assumed to be parallel to z-axis (blue arrow). Around the isocenter (yellow cross), the B_1-field rotates in the axial plane. The E-field, induced by the B_1-field, whirls in the coronal plane. In (**b**), SAR distribution patterns generated around a conductive bare or insulated wire are shown as inlets. See the text for detail.
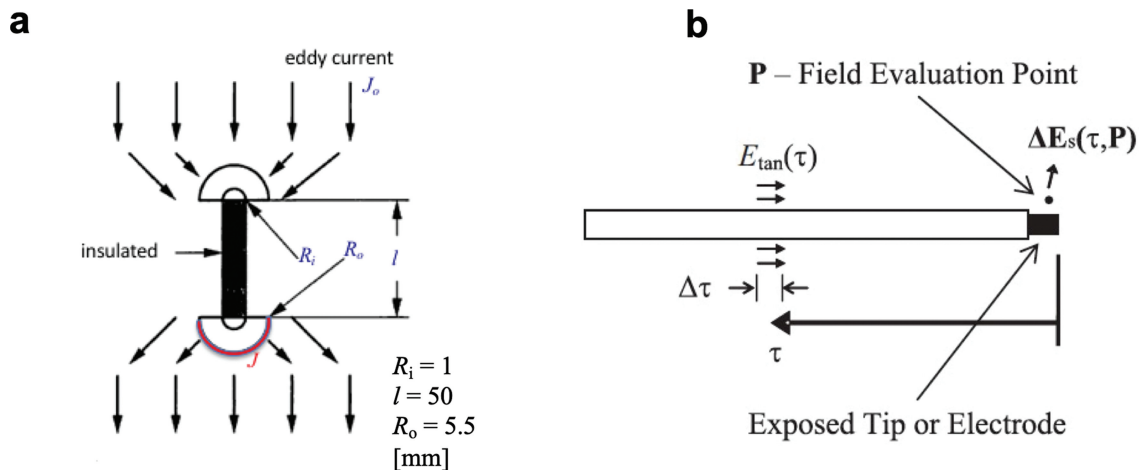

Fig. 5 Mechanism of RF-induced heating around an insulated conductive material. Two ends open (**a**) and one end open (**b**) cases are shown. In (**a**), the inflow and outflow of the conductive current are shown, for an example, of straight conductor rod covered with a thin insulation material. The measurements of the radius, R_i and length, l of the rod, as well as the radius of the half-spherical observation region, R_o, are shown in the figure. In (**b**), a lead conductor with its tip exposed to the surrounding tissue is shown. The tangential component of the electric field, E_{tan}(t) at a small segment $\Delta\tau$ of the lead contributes to the electric field $\Delta E_S(\tau, \boldsymbol{P})$ at an arbitrary point $\boldsymbol{P}$ at the lead tip. (Reprinted from reference #54 [a] and reference #55 [b])

regardless of the relative permittivity of the insulation. This insensitivity to the insulation material suggests that the heat in this case is dominated by the inflow of the electric current from the bare ends. On the other hand, in the one-end exposed case, the SAR property strongly depended on the conductor length and insulator permittivity. At a greater relative permittivity like $\varepsilon_r = 10$, the SAR peak appeared at the wire length $l = 130$ mm, close to the half wavelength in the surrounding material, but shifted to the longer side of the wire length as relative permittivity became smaller; $\varepsilon_r = 1$, $l = 210$ mm gave the highest SAR. This is because the wavelength of the 128 MHz electromagnetic field is more
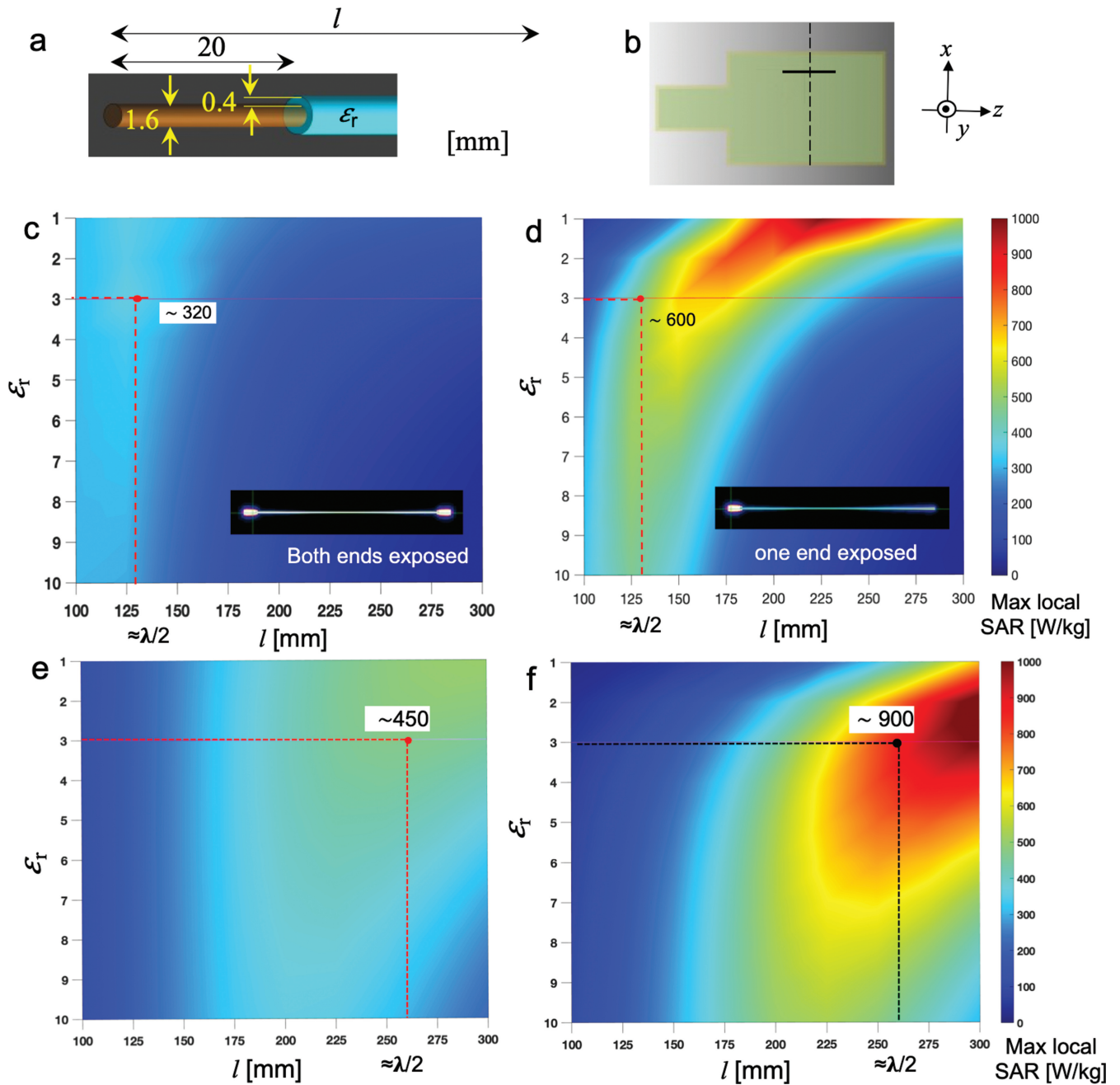
Fig. 6 Heat generation property of a lead insulated with both ends or one end left exposed. Overview of the lead model (**a**). The core is a perfect conductor with a diameter of 1.6 mm, and 20 mm at the end exposed. The other parts are insulated with a dielectric material with a thickness of 0.4 mm. The lead was placed in a lateral side of an ASTM phantom with its middle point at the z and y coordinates of the isocenter as depicted by a black bar in (**b**). Overall length and relative permittivity of the dielectric material were changed to obtain the SAR. The local SAR here was defined as the average in 1-mm³ cubic region. Resultant local maximum SAR for both ends (**c**) and one end (**d**) exposed in a 3-T scanner. Similar results in a 1.5-T scanner for both ends (**e**) and one end (**f**) exposed. ASTM, American Society for Testing and Materials; SAR, specific absorption rate.

affected and lengthened by the permittivity of the insulation material, which is thin but in the vicinity of the conductive wire. Consequently, the longer wire, which may have had a more tangential component of an electric field, induced a higher SAR than the shorter one. These are the reason why the single end exposed case was highly sensitive to the permittivity of the insulation material and the length of the conductor. At the relative permittivity $\varepsilon_r = 3$, which is often used in the insulator of AIMD leads, and with the wire length equal to the half wavelength ($l = 130$ mm) in the
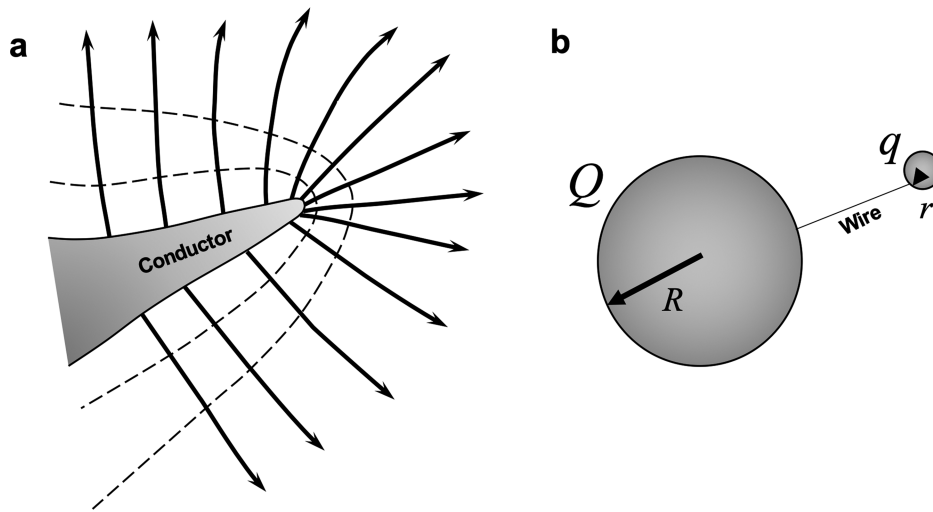
Fig. 7 Electric field distribution around a conductor with blunt and sharp parts (**a**) and a simple model to explain the reason for the distribution (**b**). In (**b**), two conductor spheres with different radii, R and r, are connected by a wire conductor. Q and q are the electric charges on the spheres. (Modified from reference #59)

phantom material, the local maximum SAR at the tip of the wire value was 600 W/kg. This value was almost twice that obtained with the case in which both ends were exposed. Similar results at 1.5T are shown in Fig 6e and 6f. Although the resonance length in the phantom material at 64 MHz is $l = 260$ mm, the SAR peak appeared to be larger at $l = 300$ mm because of the effect of the insulation material. When $\varepsilon_r = 3$ and $l = 260$ mm, the highest SAR was about 450 W/kg in the both-end exposed case, while it was about 900 W/kg in the one-end exposed case. These results tell us that the one-end exposed case yielded a much higher SAR because the entire electrical energy induced along the wire length is dissipated at the single, exposed end. In the both-end exposed case, the dissipation is somewhat diluted.

It is also known that in metal objects, sharp parts generate heat more than blunt parts. This is explained in Fig. 7.[59] That is, first, a metal object having the shape shown in Fig. 7a is approximated by a model in which a small sphere corresponding to the sharp part and a large sphere corresponding to the other part are connected by a conductive wire as depicted in Fig. 7b. Since the inside of the conductor is equipotential, all the induced charges are distributed on the surface of the conductor. Assuming that the amount of charge induced in both large and small spheres is Q and q, and the radii of both spheres are R and r, the following relationship holds because both spheres are connected by a conductor, and thus the potential ϕ is the same.

$$\phi \propto \frac{Q}{a} = \frac{q}{b} \qquad (3).$$

Based on the Gauss's law, the electric field on the surface of a spherical conductor can be obtained by dividing the surface potential by the radius of the sphere. Thus, the ratio of the electric fields E_a and E_b generated on the surfaces of both spheres can be derived as follows using the relationship in Eq. (3):

$$\frac{E_b}{E_a} = \left(\frac{q}{b^2}\right) \Big/ \left(\frac{Q}{a^2}\right) = \frac{a}{b} \qquad (4).$$

From this, we see that the ratio of the strength of the electric field is proportional to the reverse ratio of the radii. That is, the smaller the size of the sharp part is in relation to the blunt part, the stronger the electric field, and the SAR increases in proportion to the square. This is the reason why the tip of the stem driven into the femur generates heat in the artificial hip joint, for example.[60]

Relationships of SAR and $B_{1+\text{RMS}}$

The degree of heat generation as described above can be evaluated by the amount of heat per unit time and unit mass, that is, the SAR (W/kg)[5]:

$$SAR = \frac{DC}{2\rho} \boldsymbol{E} \cdot \boldsymbol{J} = \frac{DC}{2\rho} \sigma E^2 = \frac{DC}{2\rho} \frac{J^2}{\sigma} \qquad (5),$$

$$\boldsymbol{J} = \sigma \boldsymbol{E} \qquad (6),$$

where σ is conductivity of the tissue (ease of current flow) (S/m), ρ is density of the tissue (kg/m³), $\boldsymbol{E}$ is electric field (V/m), $\boldsymbol{J}$ is current density (A/m²), and DC is the abbreviation for duty cycle, which is the ratio of the RF magnetic field application time per unit time. The reason for dividing by 2 is to obtain the average value (effective value) of alternate current phenomena. Equation (6) expresses the relationship between the electric field and the current density, and gives the relationship of the third and fourth terms of Eq. (5).

Since direct measurement of the absorbed power in the human body is not possible, the whole-body average SAR is calculated or predicted in advance on the MR system and displayed on the console. Since the manufacturer decides this calculation/prediction method independently, there might be a difference in the effective SAR value among different MR systems, even when those systems displayed the same SAR values on the consoles.[61–63]

Since the SAR is used for purposes of controlling patient heating, but implants interact with the B_1 field, it is required to display the 10-s mean square (B_{1+RMS}) of the component (B_{1+}) that contributes to the excitation of the signal in the RF magnetic field (B_1) generated from the coil.[14]

$$B_{1+RMS} = \sqrt{\frac{\int_0^T (B_{1+}(t))^2 dt}{T}} \qquad (7),$$

where T is the integration time, which shall be any 10-s period over the duration of the entire sequence that produces the maximum B_{1+RMS}.

To compare the console-displayed SAR against B_{1+RMS}, whole-body averaged SAR was measured using the calorimetry method specified in ASTM F2182-11a[64] and NEMA 8[65] in two different 1.5-T and in one 3-T clinical scanners.[61] Figure 8 shows the experimental setup. An ASTM F2182 phantom containing saline solution (0.9 weight%) was covered with a styrofoam thermal insulator as shown in (a). Four channels of fiberoptic thermometer probes were placed inside and outside of the phantom as shown in (b). Channels 1 and 2 were immersed in the solution at the isocenter position and the lateral side of the phantom. Channels 3 and 4 were used to monitor the ambient temperature in the gantry.

RF irradiation was achieved using a conventional fast spin echo. The imaging conditions were set as listed in Table 1 to have a console-reported whole-body averaged SAR (hereafter, Console SAR) as 2.0 W/kg, 1.0 W/kg, or a console-reported B_{1+RMS} (hereafter, Console B_{1+RMS}) as 3.2 μT. The SAR value of 2.0 W/kg was chosen as the maximum whole-body average SAR in the normal operating mode as specified in the IEC standard.[14] The value 1.0 W/kg was simply chosen as a half of the maximum value. The B_{1+RMS} value of 3.2μT was chosen as the maximum value of the fixed parameter option: basic (FPO:B) specified in the standard.[14] When these conditions were not exactly achievable, closest conditions were set. The calorimetric measurements were performed along with the method specified in ASTM F2182-11a[66] and NEMA MS-8.[67] Before scanning, the phantom temperature was measured after equilibration with the ambient temperature. After scanning, the phantom temperature was measured after the filler was stirred sufficiently to have a uniform temperature. The total energy deposition was obtained by the following equation:

$$P_{ave} = \frac{m_{phantom} c(T_f - T_i)}{\tau} \qquad (8),$$

where $m_{phantom}$ is the phantom filler mass (= 25 kg), c is the heat capacity of the saline solution (= 4150 J/[kg·°C]), T_i is the initial temperature (°C), T_f is the final temperature (°C), and τ is the scan duration (= 30 min). The SAR was estimated by dividing the power deposition with a phantom's equivalent mass, m_{body}, by which the substantial difference between the solution phantom and a human subject, such as difference of heat conductivity and presence or absence of blood perfusion, is considered.[67]

$$SAR = \frac{P_{ave}}{m_{body}} \qquad (9).$$

The range of m_{body} can be set to 70–90 kg.[67]

The results are shown in Fig. 9.[61] The console SAR and console B_{1+RMS} were plotted against the measured SAR estimated with the equivalent mass m_{body} equal to 70 kg, which is the input weight for the sequence setup shown in Table 1. In order to match to the dimension of power, the console B_{1+RMS} values were squared and expressed in a unit of (μ T^2). In one 1.5-T scanner result shown in Fig. 9a, the console SAR was almost doubled compared with the measured SAR. Console SAR of 2.0W/kg corresponded to a measured SAR of 1.0 W/kg. This means that the console SAR was overestimating the measured SAR with enough margins. In another 1.5-T result shown in Fig. 9b, the console SAR agreed well with the measured value with the phantom's equivalent mass setting used here. In the 3-T scanner shown in Fig. 9c, the console SAR was almost three times larger than the measured value. These results demonstrate that the console SAR values in all the scanners used in this study were conservative and on the safe side.

However, these results also tell us that the actual power deposition varies largely among different scanners. In fact, the maximum SAR value attainable in the second 1.5-T scanner or the 3-T scanner was 1.4W/kg. If the two 1.5-T scanners are compared, the console SAR value of 1.0 W/kg was the result of a measured SAR of 0.55 W/kg in one scanner (Fig. 9a) but was 1.0 W/kg in another (Fig. 9b). In the 3T scanner, the same console SAR corresponded to 0.4 W/kg (Fig. 9c) according to the first-order regression line. Therefore, attention should be given to the fact that the actual power deposited into a patient body or into an IMD is not the same from one scanner to the other, even if an identical SAR value is displayed on the scanner console.

On the other hand, the relationships of the console squared B_{1+RMS} values with the measured SAR values were more consistent than those of the console SAR. Compared with the ratios between the console and measured SAR values, that is the slopes of the regression lines (0.91–2.8), those between the console B_{1+RMS} and the measured SAR
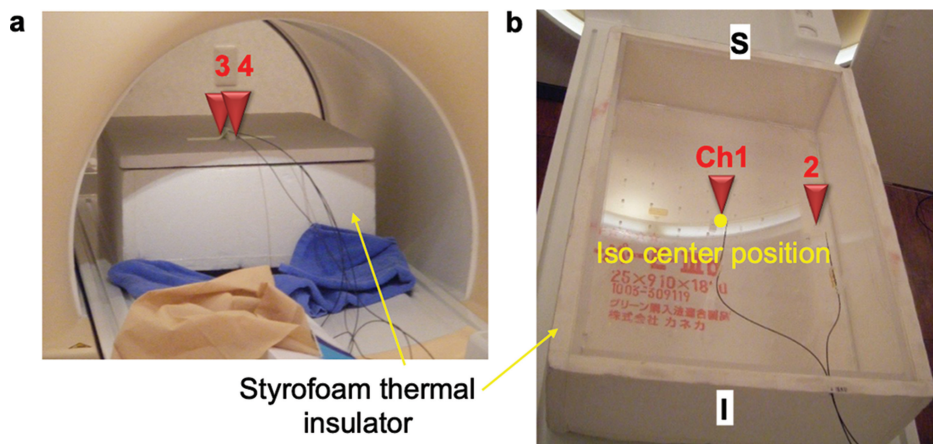
Fig. 8 An ASTM F2182 phantom containing saline solution covered with polystyrene foam thermal insulator. The outside view of the phantom in a scanner gantry (**a**). The inside view with the position of isocenter indicated by a yellow dot. (**b**). Red arrow heads with numbers denote the positions of 4-channel fiberoptic thermometer probes. ASTM, American Society for Testing and Materials. I, inferior; S, superior.

Table 1 Typical conditions of long echo train FSE sequences used for calorimetry based on ASTM F2182-11a and NEMA MS 8-2016

	Irradiation 1	Irradiation 2	Irradiation 3
Body weight (kg)	70	″	″
Console SAR (W/kg)	2*	1	1.4
B_{1+RMS} (μT)	3.72	2.64	3.2
Sequence	FSE	″	″
TR (ms)	3275	″	4425
TE (ms)	63	63	63
Echo train length	14	7	14
Echo spacing (ms)	8.4	″	″
FOV (cm)	42	″	″
Acquisition matrix	512 × 416	″	″
Number of slices	15	″	″
Slice thickness (mm)	4	″	″
Band width (Hz)	393.8	″	″
Averaging	19	10	14
Scan duration	30 m 8 s	32 m 16 s	30 m 1 s

*When this SAR condition was not reachable with the imaging parameters specified here, the closest highest SAR condition was adopted. FSE, fast spin echo; NEMA, National Electrical Manufacturers Association; SAR, specific absorption rate.

was somewhat smaller (8.6–13.3). This means that B_{1+RMS} may be a more consistent measurement of the scan condition than SAR. This is one of the reasons why B_{1+RMS} may be a more precise measurement than SAR for specifying the imaging conditions of IMDs.

Note that there were some limitations in this study. First, the weight and thermal capacity of the acryl container of the phantom was not considered in the calorimetric measurements. It is undeniable that there is an error due to not considering the mass and heat capacity of the phantom

container. Also, there was a slight difference in the imaging conditions among the three scanners because of the different limitations of parameter setting, although the values of console SAR and B_{1+RMS} were consistent.

Scan conditions and Image quality
For MR-conditional IMDs, maximum allowable values of SAR and/or B_{1+RMS} are specified as imaging conditions. Since these parameters have different physical meanings, the imaging parameters and the resultant image quality may
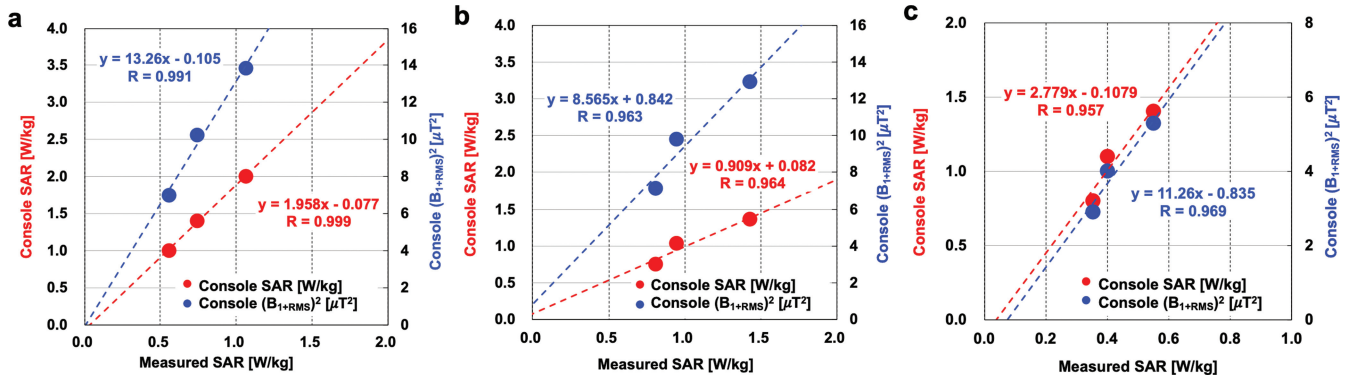
Fig. 9 Relationships between measured SAR and console SAR or console B_{1+RMS} for two different 1.5-T scanners (**a** and **b**) and a 3-T scanner (**c**). The measured SAR was obtained by dividing the calorimetry-measured power deposition by phantom's equivalent mass, m_{body} of 70 kg. The console B_{1+RMS} is squared to have a dimension $[\mu T^2]$ to be in proportion to SAR. The equations shown in the charts are the regression line and the correlation coefficient for each data set.
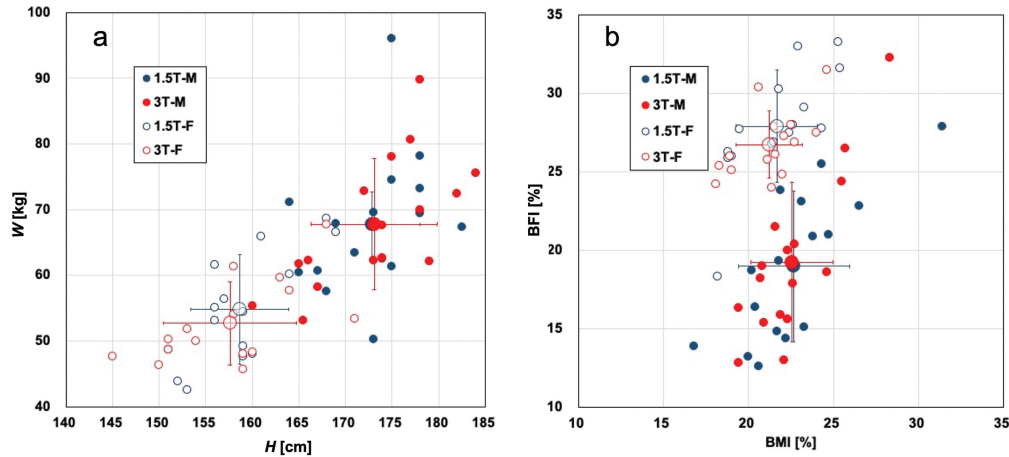

Fig. 10 Body constitution of the volunteers. Height, H [cm] versus weight, W [kg] (**a**) and body fat index, BFI [%] versus body mass index, BMI [%] (**b**) are shown for male and female volunteers at 1.5T (1.5T-M, 1.5T-F) as well as 3T (3T-M, 3T-F). The horizontal and vertical bars in each chart are the ranges of standard deviation of the data around the mean values depicted by large circles.

vary with the selection of these limiting conditions. Despite the above-mentioned variation of the measured SAR in comparison with console SAR, technicians strongly depend on the console SAR and B_{1+RMS} to come along with the package inserts. In addition, only SAR is available on some relatively old 1.5-T scanners. Deterioration of image quality stemming from the selection of these limiting factors should be avoided to guarantee sufficient clinical output. Thus, a volunteer study was conducted to evaluate the image quality, SNR, contrast-to-noise ratio (CNR), and scan duration for the same spatial coverage under different whole-body SAR and B_{1+RMS} settings.[61] Thirty healthy volunteers with various body constitutions (Fig. 10) were examined at 1.5T or 3T[61] under the approval from the institutional review board.[61] Body fat index, BFI (%) (= $W_F/W \times 100$) and body mass

index, BMI (= W/H^2) were obtained by a commercially available body composite meter (HBF-701, Omron Corp., Kyoto, Japan).[61] Here, W_F is fat weight [kg] estimated by electrical impedance measurement, W is body weight (kg), and H is height (m) self-reported by each volunteer.

Routinely used imaging sequences and parameters were used. As examples, the imaging conditions for brain T1- and T2-weighted images (T1W and T2W), and short-axis cardiac cine imaging (Short ax cine) are summarized in Table 2. Twenty-four slices were taken for the brain scans, while a single slice was taken for the cardiac cine scans. All the sequences were set to have console-displayed RF power values for SAR of 2.0 and 1.0 W/kg, as well as B_{1+RMS} of 3.2 µT by adjusting the imaging parameters such as TR, echo train length, and flip angle. When these conditions were not

Table 2 Scan conditions for the volunteer study

|	1.5T			3T		
	Brain		Cardiac	Brain		Cardiac
	T1W	T2W	Short-axis cine	T1W	T2W	Short-axis cine
Slice orientation	Axial	Axial	Oblique	Axial	Axial	Oblique
Sequence	SE	FSE	SSFP	SE	FSE	SSFP
TR (ms)	450	4800	3.2–3.6	450–470	4000	2.9–4.1
TE (ms)	12	100	1.7–1.8	11	80	1.5–1.8
FA (degree)	90, 180	90, 180	55–60	90, 180	90, 180	46–65
Echo train length	1	13	14	1	13	8
FOV (cm)	24 × 24	24 × 24	38 × 38	24 × 24	24 × 24	38 × 38
Acquisition matrix	304 × 244	325 × 285	192 × 196	288 × 231	352 × 317	128 × 240
Number of slices	24	24	2	24	24	1
Slice thickness (mm)	5	5	8	5	5	8
Band width (Hz)	181	182	868	163	202	2830
Averaging	1	1	1	1	1	1
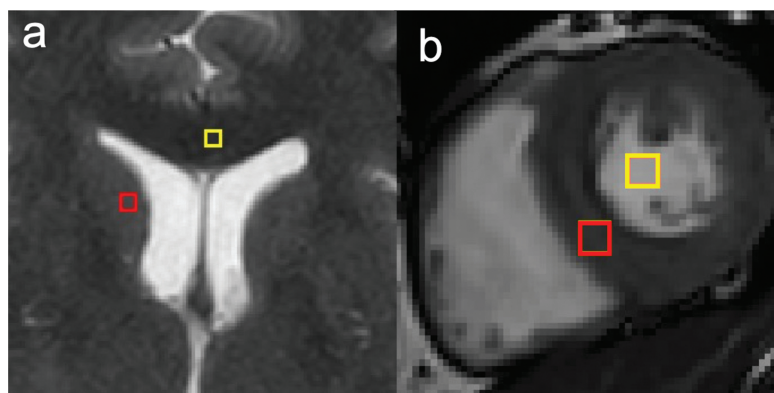
Fig. 11 ROI settings for SNR and CNR evaluation in the brain (**a**) and heart (**b**) in the volunteer study. In the brain, the ROI was placed in the caudate nucleus (red square in (**a**)) for SNR calculation, and another ROI was placed in the corpus callosum (yellow square) for CNR calculation. For cardiac imaging, the ROI was placed in the septal myocardium (red square in (**b**)) and in the blood in the left ventricle (yellow square).

exactly achievable, closest conditions were set. The number of slices of SNR and CNR was evaluated for quantitative assessment of the images by positioning the ROI as shown in Fig. 11. The SNR in the brain was obtained as the ratio of the mean signal intensity in the ROI taken in the caudate nucleus head versus standard deviation in the background noise signal, whereas the CNR was obtained as the ratio of the mean signal intensity difference between the caudate nucleus and corpus callosum against the background noise. Similarly, the SNR in the cardiac cine imaging was calculated as the ratio between the mean signal intensity in the ROI in the septal myocardium and the background noise. The CNR was

calculated as the ratio of the mean signal intensity difference between the septal myocardium and the blood in the left ventricle.

Figure 12 shows the examples of the results.[61] The console SAR and B_{1+RMS} values, scan durations, image SNR, and CNR for brain and cardiac imaging for all the volunteers at 1.5T are shown. Note that the maximum available setting of whole-body average SAR for brain imaging was 1.6 W/kg. At this SAR setting, the console displayed B_{1+RMS} was about 3.4 µT, which was almost equivalent to 3.2 µT as shown in Fig. 12a. The scan duration for brain T1W imaging was about 1.6 times longer in SAR

1.0 case compared with SAR 1.6 and B$_{+RMS}$ 2.0 cases as shown in Fig 12b. In brain T2W and cardiac short-axis cine imaging, the scan durations were almost the same. There was no significant difference in SNR and CNR in each of the brain and cardiac images. Examples of the images are shown in Fig. 13 together with the image quality scored by three expert radiologists. In these examples for brain T2W and cardiac short axis cine images, apart from the fact that the image acquisition times were almost the same for the different power settings, the image quality scored by three radiologists was almost the same.

At 3T, the overall trends were slightly different. For brain T2W imaging, the highest attainable B_{1+RMS} was 2.07 µT, which corresponded to the whole-body average SAR of around 2.5W/kg as shown in Fig. 14a. A similar tendency was observed in the T1W imaging in that the highest attainable B_{1+RMS} was 2.26 µT, which corresponded to the average SAR of around 2.5W/kg. The image acquisition time was prolonged when an SAR of 1.0 W/kg was used from the other power settings for both T1W and T2W imaging, as shown in Fig. 14b. SNR and CNR were not significantly different for different power setting as shown in Fig. 14c and 14d. In fact, the image quality scores were also similar in the three different power settings, although the individual difference among the three radiologists was remarkable, as shown in Fig. 15d. As is shown in Fig. 14e for cardiac imaging, the SAR values determined by B_{1+RMS} setting largely deviated. Interestingly, the image acquisition times do not differ in the three power settings as depicted. The image quality scores assessed by each radiologist were similar, although the individual difference was also apparent as in Fig. 15h.

These results demonstrate that image quality can be maintained even when the power setting is low. If the total acquisition time for each patient is allowable, it will be possible to lower the power setting to the limit required for the particular IMD.

Future Directions

Feasibility of RF heating tests based on MR thermometry

In current safety test methods, SAR generated by the existence of an IMD is estimated by measuring temperature with a fluoroptic thermometer at a few points around the device.[38,43] Such a point measurement technique gives only limited information about the temperature and SAR distributions. On the other hand, MR thermometry is known to be useful for monitoring tissue temperature change distribution during thermal therapies.[68,69] The most widely used technique is proton resonance frequency (PRF) shift. It is based on the temperature dependence of the shielding effect of an electron cloud around protons, induced by a change in electrical force strength of hydrogen bonding.[70–73] To observe the PRF shift in a practical spatiotemporal resolution, a change in phase of a complex signal obtained by gradient echo-based sequences, including echo planar, is obtained. Since such phase distribution measurement is highly sensitive to susceptibility effect and magnetic field inhomogeneity, temperature distribution imaging in the vicinity of an IMD is problematic.[74] As a result, several studies have been conducted for overcoming this problem.[74–80] Pfeil et al. proposed the use of proton MRS for thermometry at the tip of pacing leads in a porcine myocardium ex vivo.[76] The measurement was based on the chemical shift difference between protons of water and N-methyl protons of creatine/phosphocreatine (Cr/PCr) and trimethylamine (TMA). Detti et al. evaluated the temperature increase in a copper wire of 0.3 m ($\lambda/16$) in length in a homogeneous agar gel phantom using T1-weighted signal intensity of true fast imaging with a steady-state free precession (true FISP) sequence at 1.5T.[75] They prepared another 1.7-m section of wire (6 ramda/16) placed near the gantry wall to be connected to the shorter wire in the phantom to create an large induction current in the entire wire structure. Since the wire was made of copper, whose susceptibility is close to that of water (~ -9.0 ppm), the artifact created by the shorter wire alone was small when not connected to the longer one, while it was remarkable when connected. In order to reduce the effect of such an artifact, they adopted a correlation estimation to predict the temperature elevation in the region of signal void induced by the artifact. As a result, a temperature map around the wire was obtained.

Gensler et al. applied fast T1 mapping with inversion recovery snapshot Fast Low-Angle Shot (FLASH) sequence to the hydroxyethyl cellulose (HEC) gel and porcine tissue with a 20-cm-long copper wire inside.[77] Since T1 mapping is less sensitive than phase mapping for PRF to susceptibility distribution, the artifact around the wire was reduced by revising the slice orientation. The resultant T1 mapping technique successfully converted to a temperature map.

Weber et al. devised the T1 mapping technique in conjunction with a 2D multispectral imaging (2D-MSI) technique with single-shot fast spin echo.[74] As is depicted in Fig. 16a and 16b, a set of 12-slice 2D fast spin echo was obtained in the first acquisition by keeping the slice gradient strength constant while changing the frequency offset of a 90-degree pulse. In the second acquisition, an identical slice set was obtained with the gradient of identical intensity but with opposite polarization. By adding the images in the two acquisitions, the effect of slice gradient, which is the most significant source of artifacts, was effectively reduced as shown in Fig. 16c. The resultant temperature maps were compared with those obtained by means of a conventional gradient-echo-based PRF technique, exhibiting the superiority of the proposed T1 approach as shown in Fig. 17.

An alternative approach to reducing the effect of artifact is to use an ultrashort echo time (UTE) technique. Griffin et al. utilized their own UTE sequences to quantify the electric current in the ASTM phantom.[79] The current value in each voxel was converted to SAR, which was
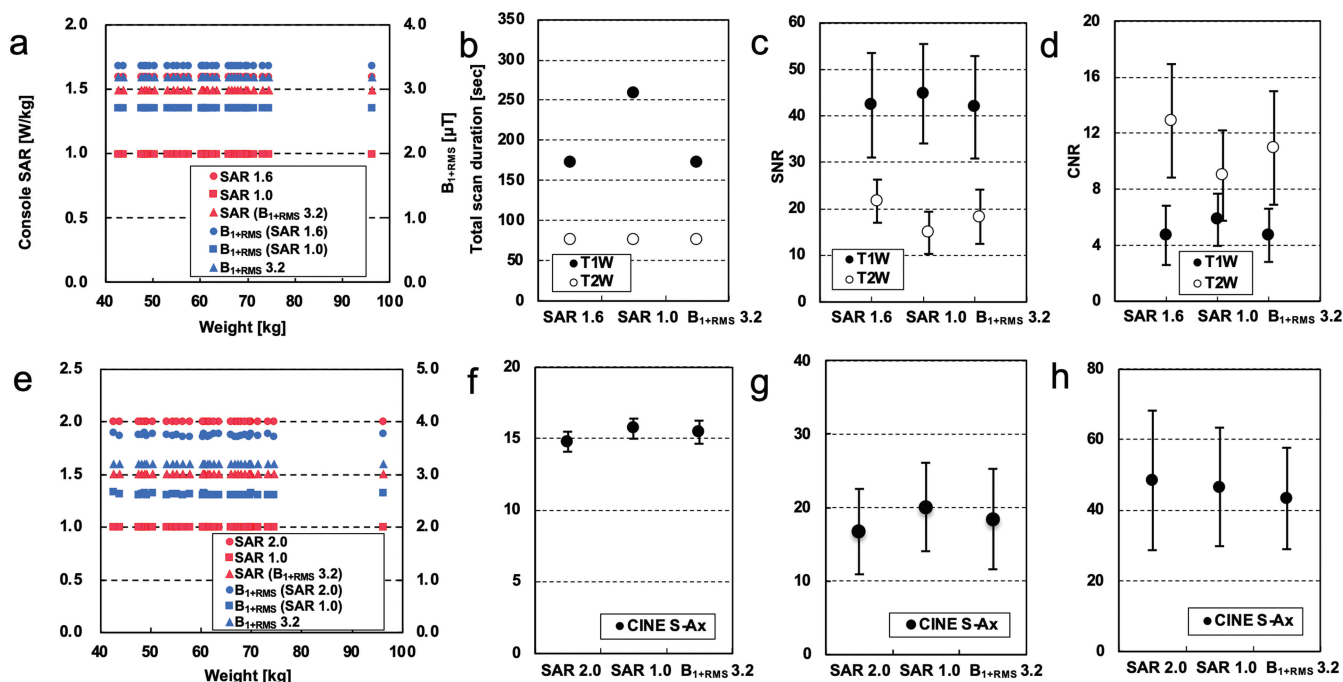
Fig. 12 Power settings (**a**), scan durations (**b**), SNR (**c**), and CNR (**d**) for brain imaging in 30 volunteers including both males and females at 1.5T. The chart (**a**) is shown only for T2W for simplicity but was similar for T1W. Note that the maximum available setting of whole-body average SAR was 1.6 W/kg for brain imaging, and thus the corresponding legends and axis label is "SAR 1.6". The similar results for cardiac short-axis cine (CINE S-Ax) imaging (**e–h**) are also shown.
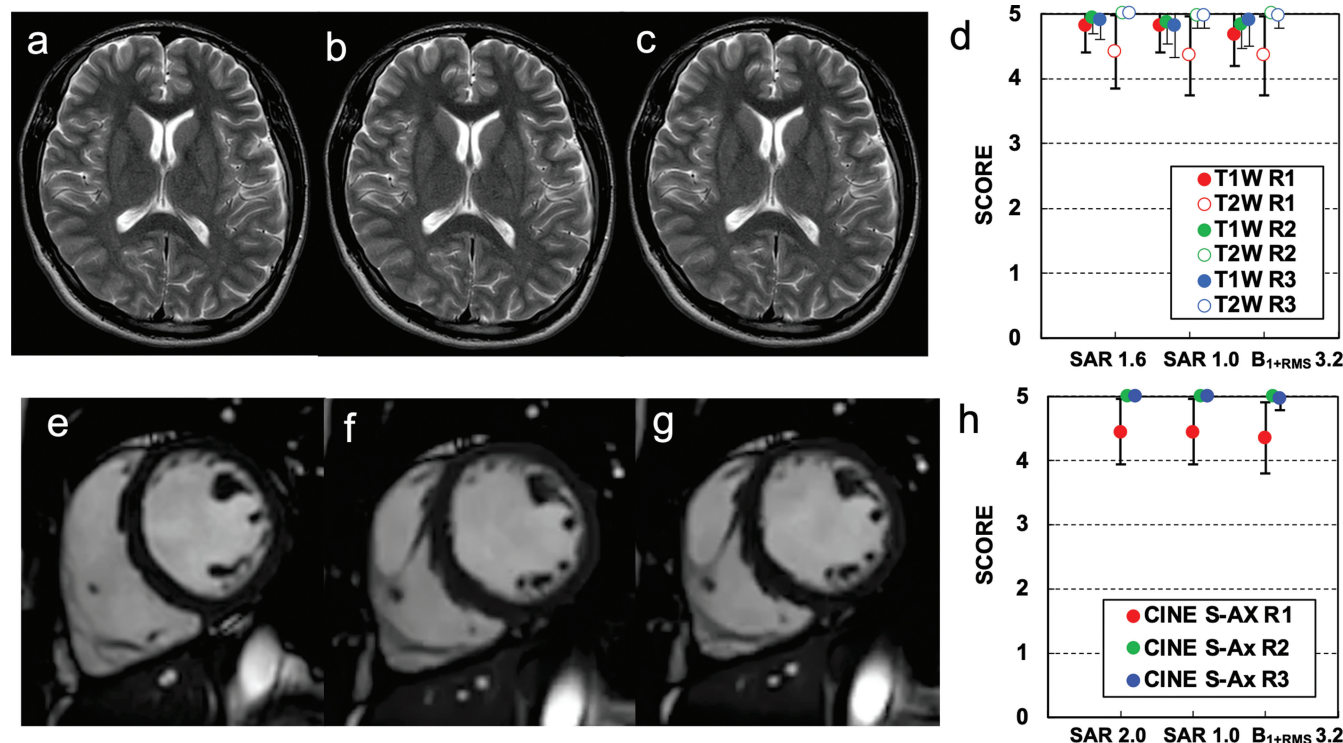

Fig. 13 Example images of brain T2W images (**a–c**) of a male volunteer (34 yo, 174 cm, 68 kg, BMI = 22.3%) and the image quality for T1W and T2W images of the 30 volunteers at 1.5T scored by three expert radiologists (R1, R2, and R3) (**d**). The error bars are the range of standard deviations in the scores by each radiologist for all the volunteers. Example images of short-axis cine cardiac images (**e–g**) from the identical volunteer and the scores (**h**) are also shown.
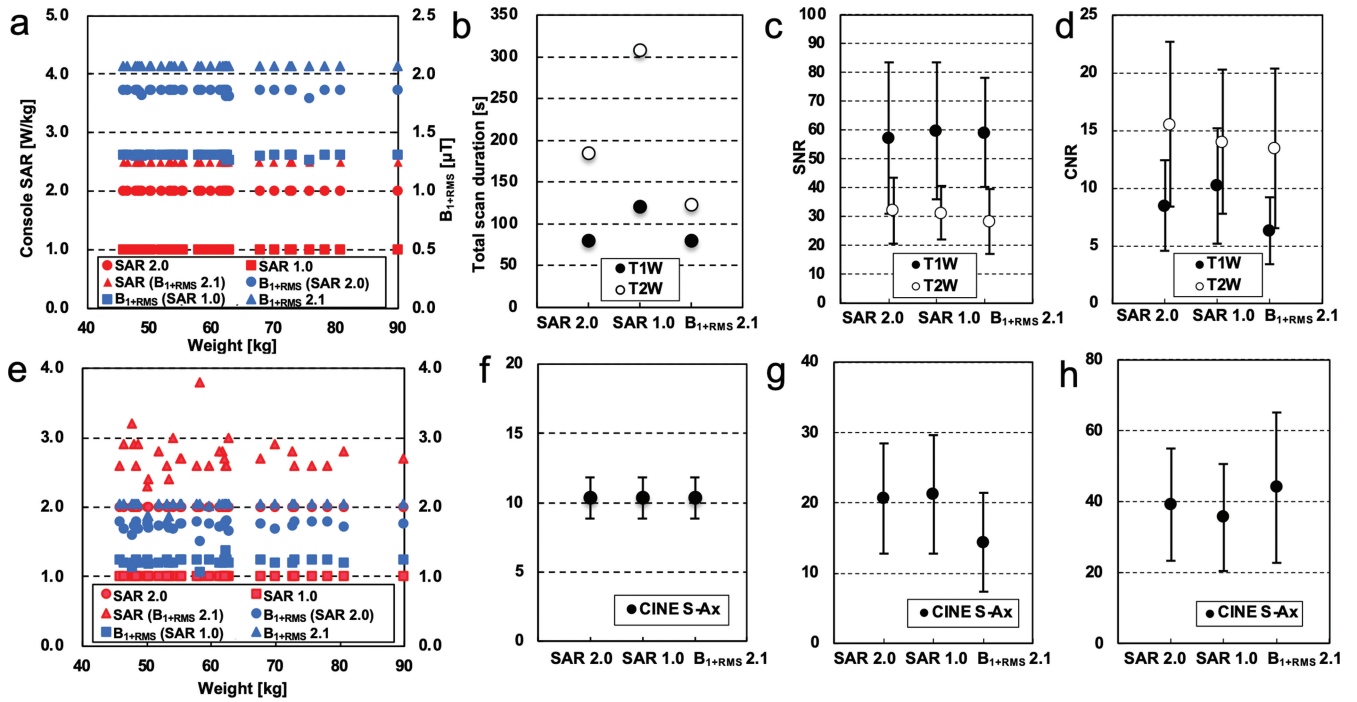
Fig. 14 Power settings (**a**), scan durations (**b**), SNR (**c**), and CNR (**d**) for brain imaging in 30 volunteers including both males and females at 3T. The chart (**a**) is shown only for T2W for simplicity. Although maximum available setting of B_{1+RMS} was 2.07 (μT) for T2W and 2.26 (μT) for T1W, the notation "B_{1+RMS} 2.1" is used for the legends and horizontal axis. Similar results for cardiac short-axis cine (CINE S-Ax) imaging (**e–h**) are also shown. Although the maximum available B_{1+RMS} was 2.05 (μT), "B_{1+RMS} 2.1" is used for the relating legends and axis.
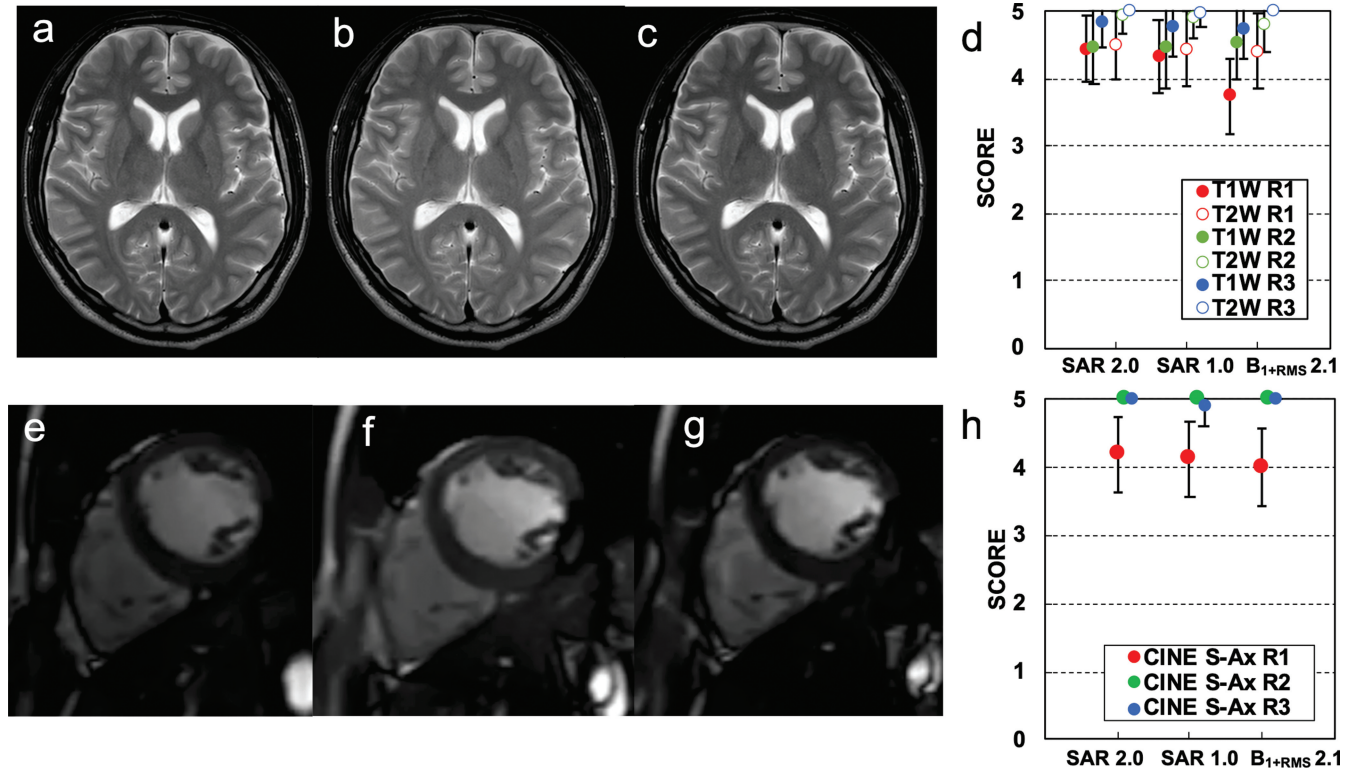

Fig. 15 Example images of brain T2W images (**a–c**) of a male volunteer (34 yo, 174 cm, 68 kg, BMI = 22.3%) and the image quality for T1W and T2W images of the 30 volunteers at 3T scored by three expert radiologists (R1, R2, and R3) (**d**). The error bars are the range of standard deviations in the scores by each radiologist for all the volunteers. Example images of short-axis cine cardiac images (**e–g**) from the identical volunteer and the scores (**h**) are also shown.
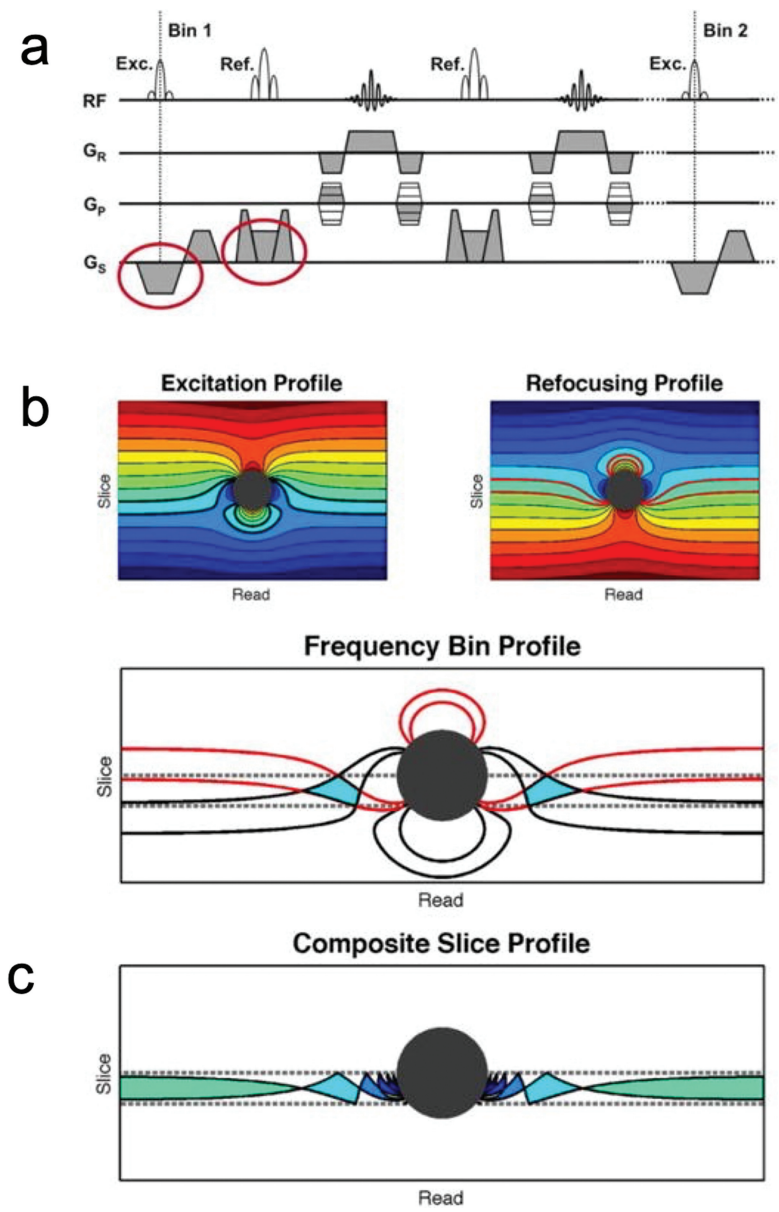
Fig. 16 Pulse sequence diagram of the 2DMSI sequence, including the first two echoes of the spin echo train (**a**). The slice selection gradient is inverted for the excitation pulse (see red circles). Slice profiles for excitation and refocusing with the inverted slice selection gradient (**b**). The overlap of both profiles yields the profile of the frequency bin, which contributes signal. The different colors mean different bins. The overlay of all frequency bins shows the individual contributions to the composite slice profile, which can be improved by adjusting the overlap between adjacent bins (**c**). 2DMSI, 2D multispectral imaging. (Reprinted from reference #74)

then used to estimate the temperature around a guide wire based on the Penne's bioheat transfer equation.[51] They compared the UTE technique with the conventional gradient echo-based current imaging. Although this approach is an indirect way of characterizing temperature distribution, the UTE technique sufficiently suppressed the artifact.

Such MR temperature imaging techniques are evolving and might be used for assessing RF-induced heating in the near future.

Evaluation of tissue damage
In future revisions of the IEC IEC60601-2-33, the adoption of the following Cumulative Equivalent Mins at 43°C (CEM43)[81] is being considered to quantify tissue damage caused by RF heating[14]:

$$\text{CEM43} = \int_0^t R^{(T[\tau]-43)} d\tau \qquad (10),$$

where T is the temperature (°C), t is the temperature measurement time (min), and R is an experimentally determined constant with the following values:

$$R = \begin{cases} 0.25 \ (\text{T} < 43°C) \\ 0.5 \ (\text{T} \geq 43°C) \end{cases} \qquad (11).$$

CEM43 indicates how many minutes of warming of tissue at a certain temperature correspond to warming at 43°C, and if this is shorter than 240 min, protein denaturation and thus cell death do not occur, resulting in negligible tissue damage. It should be noted that CEM43 is an index at the cellular level and does not directly regulate safety at the tissue or
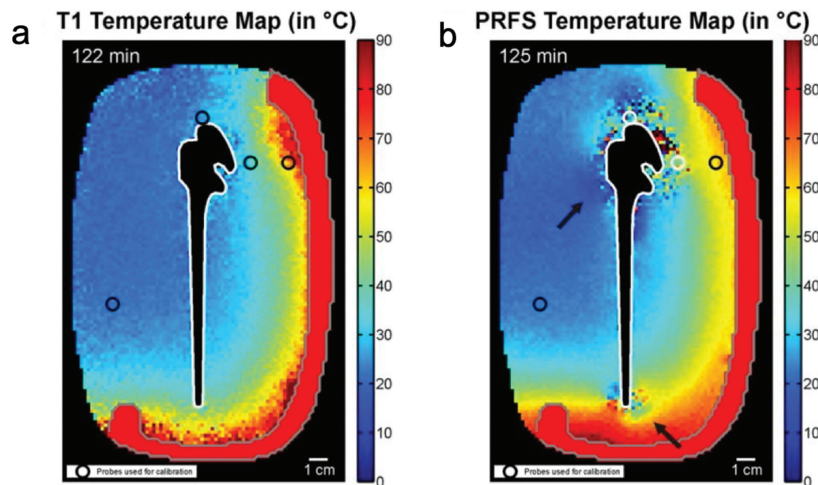
Fig. 17 Absolute temperature maps in an agarose gel phantom based on the T_1 measurements (**a**) and the PRFS measurements (**b**) at comparable time points. The temperature in the area of the heat source shown as gray closed lines over the red regions was set to the temperature of the heating water. Black circles indicate the location of the temperature probes used for calibration. The arrows point to areas of inconsistent temperature pattern in the PRFS temperature map. PRFS, proton resonance frequency shift. (Reprinted from reference #74)

organ level.[82] The IEC60601-2-33 standard is scheduled for revision in 2022.[83] The NEMA MS14 standard defines heat generation on the RF coil surface.[84] Since skin temperature must not exceed 41°C without justification, the coil surface temperature elevation should be less than 4°C assuming that the normal body temperature is 37°C. Based on these two standards, the MR scanner safety precautions about body heating will be further clarified.

Cardiac device combination

Until now, MR-conditional AIMDs have been approved by the FDA and the PMDA with limits on the combination of the main generator unit (power supply) and lead wires. In particular, cardiac devices were most intensively evaluated in terms of MR safety.[85–93] When a generator has to be replaced for battery replacement, the most suitable generator product may be selected according to the patient's situation at that time. For cardiac devices, in particular, the connection interface between the lead and the generator is standardized as IS-1, based on the ISO 5841-3 standard,[94] and thus, it is common to replace the generator with a product manufactured by a company that is different from the one who produced the original. In this case, even if the lead and the generator are both MR-conditional, their combination is not regarded as such, because it is different from the approved combination.

In recent years, in North America and Europe, reports and recommendations have been made about safety considerations for MRI examinations and for patients wearing MR non-conditional devices.[95–100] However, using other companies' products for generator replacement has not yet been sufficiently examined in these reports. Therefore, the Medical Devices Department of the National Institute of Health Sciences in Japan has launched an MHLW project on post-marketing safety measures for safe and effective use of new medical devices. As a part of this project,

investigation on the cardiac device combination problem is in progress with the Japanese Society of Magnetic Resonance Medicine (JSMRM), the Japan Radiological Society (JRS), and the Japanese Heart Rhythm Society (JHRS). Other research group is also working on the issue and has developed a technique to measure the input impedance properties of multiple cardiac devices, including PM, ICD, and CRT-D.[101] Furthermore, the same group measured the total input impedance when the generator and lead of different manufacturers were combined[102] to find the contribution of the generator impedance to the total input impedance. They examined two lead products of different lengths from four different manufacturers (8 leads in total) in combination with generator products from the same four companies; two lead products were approved for use in combination. The results show that the contribution of the generator to the total impedance is around 1% to 6%, and thus the total impedance is almost entirely determined by the lead. Since the RF heating property at the lead tip was dominated by the lead impedance, combining a generator from a different manufacturer might not have an effect on RF heating property. In addition to this evaluation of impedance, direct measurement of heat generation based on phantom experiments is necessary to proceed with the safety assessment of different product combinations.

In addition, the issues of abandoned leads for cardiac devices, as well as the safety of epicardial leads commonly used for pediatric patients, have to be resolved. As described in the discussion for Fig. 6, when an insulated conductor such as a lead is present in the body, the heat generation characteristic partly depends on whether the conductor is exposed at both ends or at one end only. Detailed modeling to simulate the lead configuration and trajectory is therefore required. Although a cap at the distal end is essential to prevent fluid infiltration into the space between the coating

and the conductor,[103] the material of the cap has to be investigated to determine whether it should be dielectric or conductive.

For pediatric patients, epicardial leads are often used instead of transvenous leads to accommodate body growth. When RF heating is generated at the tip of a lead that has been inserted in or in contact with the myocardium from the epicardial side, the cooling effect of blood pooling is not expected. Therefore, the thermal damage to the tissue might become more serious, unlike a transvenous lead with the tip on the endocardial side. Furthermore, the possibility of increased heating as a result of following a trajectory different from that of the transvenous lead cannot be denied. Regarding cardiac devices, the above-mentioned issues have to be considered for PM, ICDs, CRT-D, and CRT-P.

Conclusion

This paper focused only on some major issues that are still considered outstanding for MR safety. The first half of the paper discussed the concept of the upper limit of the spatial gradient of the magnetic flux density of the static magnetic field that determines the magnetic displacement force, as well as the factors for RF-induced heating, including the inflow and outflow of current, antenna effect, and standing wave. The differences of console SAR and B_{1+RMS} for each model of MR scanner were demonstrated based on calorimetric measurement. In addition, the relationships between these thermal indicators and image quality were discussed. In the latter half, important future issues were discussed. Feasibility of evaluation of RF-induced heating with MR thermometry, as well as the meaning of CEM43 that is scheduled to be introduced in the next version of the IEC standard for evaluating tissue thermal damage, was discussed. Finally, the safety issues associated with cardiac devices when combining with different generator and lead products, residual lead, and epicardial leads for children were described.

As we are in an aging population, the use of minimally invasive treatments will become more pervasive for maintaining people's quality of life, and thus, the use of IMDs will become more common in routine medical care. In parallel, further MR safety issues will have to be considered. It would be an unexpected pleasure if this paper contributes for the understanding of MR safety now and in the future.

Acknowledgment

Conflicts of Interest

References

1. Safety Evaluation Committee Japanese Society for Magnetic Resonance in Medicine. MRI safety concept 3rd ed. Tokyo: Gakken Medical Shujun Sha, 2021. (in Japanese)
2. Motegi Y, Furuse M, Sasho K, et al. Study on safety in NMR clinical examination. Journal of NMR Medicine 1983; 3:89–96.
3. Arimizu N, Kamei H, Suzuki R, et al. Questionnaire survey on changes in physical condition and morbidity of researchers using high magnetic field devices. Journal of NMR Medicine 1984; 4:93–106.
4. Athey TW. FDA regulation of the safety of MR devices: past, present, and future. Magn Reson Imaging Clin N Am 1998; 6:791–795.
5. International Electrotechnical Commission (IEC). IEC60601-2-33 Ed. 1.0. Medical electrical equipment - Part 2-33: Particular requirements for the basic safety and essential performance of magnetic resonance equipment for medical diagnosis. Geneva:IEC, 1995.
6. Food and Drug Administration (FDA). Magnetic resonance diagnostic device; panel recommendation and report on petitions for magnetic resonance reclassification and codification of reclassification—Final rule. Fed Regist 1989; 54:5077–5078.
7. National Electrical Manufacturers Association (NEMA). NEMA MS 7-1993 (rev 1998). Measurement procedure for time varying gradient fields (dB/dt) for magnetic resonance imaging systems. Arlington:NEMA, 1993.
8. National Electrical Manufacturers Association (NEMA). NEMA MS 8-1993 (rev 2016). Characterization of the specific absorption rate for magnetic resonance imaging systems. arlington:NEMA, 1993.
9. Och JG, Clarke GD, Sobol WT, Rosen CW, Mun SK. Acceptance testing of magnetic resonance imaging systems: Report of AAPM nuclear rnagnetic resonance Task Group No. 6. Med Phys 1992; 19:217–229.
10. Shellock F. Magnetic resonance procedures: health effects and safety. New York:CRC Press, 2000. 268-269.
11. Kanal E, Shellock FG, Talagala L. Safety considerations in MR imaging. Radiology 1990; 176:593–606.
12. Kanal E, Borgstede JP, Barkovich AJ, et al. American College of Radiology: White paper on MR safety. AJR Am J Roentgenol 2002; 178:1335–1347.
13. International Electrotechnical Commission (IEC). IEC60601-2-33: 2010. Medical electrical equipment - Part 2-33: Particular requirements for the basic safety and essential performance of magnetic resonance equipment for medical diagnosis. Geneva:IEC, 2010.

14. International Electrotechnical Commission. IEC60601-2-33 Ed. 3.2. Medical electrical equipment - Part 2-33: Particular requirements for the basic safety and essential performance of magnetic resonance equipment for medical diagnosis. Geneva:IEC, 2015.

15. Glover PM, Cavin I, Qian W, Bowtell R, Gowland PA. Magnetic-field-induced vertigo: a theoretical and experimental investigation. Bioelectromagnetics 2007; 28:349–361.

16. Schenck JF, Dumoulin CL, Redington RW, Kressel HY, Elliott RT, McDougall IL. Human exposure to 4.0-tesla magnetic fields in a whole-body scanner. Med Phys 1992; 19:1089–1098.

17. Theysohn JM, Kraff O, Eilers K, et al. Vestibular effects of a 7 Tesla MRI examination compared to 1.5 T and 0 T in healthy volunteers. PLoS One 2014; 9:e92104.

18. van Nierop LE, Slottje P, Kingma H, Kromhout H. MRI-related static magnetic stray fields and postural body sway: a double-blind randomized crossover study. Magn Reson Med 2013; 70:232–240.

19. Panych LP, Madore B. The physics of MRI safety. J Magn Reson Imaging 2018; 47:28–43.

20. Davis PL, Crooks L, Arakawa M, McRee R, Kaufman L, Margulis AR. Potential hazards in NMR imaging: heating effects of changing magnetic fields and RF fields on small metallic implants. AJR Am J Roentgenol 1981; 137:857–860.

21. Woods TO. Standards for medical devices in MRI: present and future. J Magn Reson Imaging 2007; 26:1186–1189.

22. Dempsey MF, Condon B, Hadley DM. Investigation of the factors responsible for burns during MRI. J Magn Reson Imaging 2001; 13:627–631.

23. Winter L, Seifert F, Zilberti L, Murbach M, Ittermann B. MRI-related heating of implants and devices: a review. J Magn Reson Imaging 2021; 53:1646–1665.

24. Yang E, Suzuki M, Nazarian S, Halperin HR. Magnetic resonance imaging safety in patients with cardiac implantable electronic devices. Trends Cardiovasc Med 2021 Aug 9. [Epub ahead of print]

25. Oh MY, Hodaie M, Kim SH, Alkhani A, Lang AE, Lozano AM. Deep brain stimulator electrodes used for lesioning: proof of principle. Neurosurgery 2001; 49:363–367;discussion 7–9.

26. Kalin R, Stanton MS. Current clinical issues for MRI scanning of pacemaker and defibrillator patients. Pacing Clin Electrophysiol 2005; 28:326–328.

27. Wagner JH, Ernst A, Todt I. Magnet resonance imaging safety of the Vibrant Soundbridge system: a review. Otol Neurotol 2011; 32:1040–1046.

28. Chow GV, Nazarian S. MRI for patients with cardiac implantable electrical devices. Cardiol Clin 2014; 32:299–304.

29. Tsai LL, Grant AK, Mortele KJ, Kung JW, Smith MP. A practical guide to MR imaging safety: What radiologists need to know. Radiographics 2015; 35:1722–1737.

30. Aissani S, Laistler E, Felblinger J. MR safety assessment of active implantable medical devices. Radiologe 2019; 59 (Suppl1):40–45.

31. Al-Dayeh L, Rahman M, Venook R. Practical aspects of MR imaging safety test methods for MR conditional active implantable medical devices. Magn Reson Imaging Clin N Am 2020; 28:559–571.

32. Guerrini L, Mazzocchi S, Giomi A, Milli M, Carpi R. An operational approach to the execution of MR examinations in patients with CIED. Radiol Med 2020; 125:1311–1321.

33. Watson RE Jr, Edmonson HA. MR safety: Active implanted electronic devices. Magn Reson Imaging Clin N Am 2020; 28:549–558.

34. Jung JI. Magnetic resonance imaging for patients with cardiac implantable electronic devices: Reduced concerns regarding safety, but scrutiny remains critical. Korean Circ J 2016; 46:765–767.

35. American Society for Testing and Materials (ASTM) International. F2052-00. Standard test method for measurement of magnetically induced displacement force on medical devices in the magnetic resonance environment. West Conshohocken:ASTM, 2000.

36. American Society for Testing and Materials (ASTM) International. F2052-15. Standard test method for measurement of magnetically induced displacement force on medical devices in the magnetic resonance environment. West Conshohocken:ASTM, 2015.

37. American Society for Testing and Materials (ASTM) International. F2213-17. Standard test method for measurement of magnetically induced torque on medical devices in the magnetic resonance environment. West Conshohocken: ASTM, 2017.

38. American Society for Testing and Materials (ASTM) International. F2182-19e2. Standard test method for measurement of radio frequency induced heating near passive implants during magnetic resonance imaging. West Conshohocken:ASTM, 2019.

39. American Society for Testing and Materials (ASTM) International. F2119-07 (reapproved 2013). Standard test method for evaluation of MR image artifacts from passive implants. West Conshohocken:ASTM, 2013.

40. American Society for Testing and Materials (ASTM) International. F2503-20. Standard practice for marking medical devices and other items for safety in the magnetic resonance environment. West Conshohocken:ASTM, 2020.

41. American Society for Testing and Materials (ASTM) International. https://www.astm.org/products-services/standards-and-publications.html. (Accessed: December 11, 2021)

42. International Standard Organization (ISO). TS10974 1st ed. Assessment of the safety of magnetic resonance imaging for patients with an active implantable medical device. Geneva: ISO, 2012.

43. International Standard Organization (ISO). TS10974 2nd ed. Assessment of the safety of magnetic resonance imaging for patients with an active implantable medical device. Geneva: ISO, 2018.

44. ISO. TC150/SC6/JWG2, https://www.iso.org/member/1835.html. (Accessed: December 11, 2021)

45. IEC. SC62B/JWG1, https://www.iec.ch/ords/f?p=103:14:505256997034184::::FSP_ORG_ID,FSP_LANG_ID:2475,25#. (Accessed: December 11, 2021)

46. Japanese Society of Magnetic Resonance in Medicine (JSMRM). Safety information 2021. https://www.jsmrm.jp/modules/guideline/index.php?content_id=1. (in Japanese) (Accessed: December 11, 2021)

47. Gardner J. Mag Resource. https://magresource.com/?gclid=EAIaIQobChMI7oqQ7d6u9AIVTj5gCh12cQ9pEAAYASAAEgL2BfD_BwE. (Accessed: December 11, 2021)

48. Shellock FG. Shellock R & D Services 2021. http://www.mrisafety.com/. (Accessed: December 11, 2021)

49. Medie CO. Ltd. MR safety information search system for implantable medical devices. https://www.medie.jp/en/solutions/mri. (Accessed: December 11, 2021)

50. World Health Organization (WHO). Medical device regulations: Global overview and guiding principles. World Health Organization, 2003.

51. Nyenhuis JA, Park SM, Kamondetdacha R, Amjad A, Shellock FG, Rezai AR. MRI and implanted medical devices: basic interactions with an emphasis on heating. IEEE T Device Mat Re 2005; 5:467–480.

52. Yee KM. Oxygen cylinder kills South Korean man in MRI accident 2021. https://www.auntminnie.com/index.aspx?sec=ser&sub=def&pag=dis&ItemID=133794. (Accessed: December 11, 2021)

53. Bulte DP. The pursuit of hysteresis in polycrystalline ferromagnetic materials under stress. IEEE Trans Magn 2009; 45:83–87.

54. Smith C, Nyenhuis J, Kildishev A. Health effects of induced electric fields: Implications for metallic implants. In: Shellock F, Bradley W, eds. Magnetic resonance procedures health effects and safety. Boca Raton:CRC Press, 2000. 393-413.

55. Park SM, Kamondetdacha R, Nyenhuis JA. Calculation of MRI-induced heating of an implanted medical lead wire with an electric field transfer function. J Magn Reson Imaging 2007; 26:1278–1285.

56. Tokaya JP, van den Berg CAT, Luijten PR, Raaijmakers AJE. Explaining RF induced current patterns on implantable medical devices during MRI using the transfer matrix. Med Phys 2021; 48:132–141.

57. Calcagnini G, Triventi M, Censi F, et al. In vitro investigation of pacemaker lead heating induced by magnetic resonance imaging: role of implant geometry. J Magn Reson Imaging 2008; 28:879–886.

58. Kuroda K, Yatsushiro S, Sato A, Mukai K, Endo D. After flowing in the conductor, the current flow out and spreads rapidly, when it reaches the opposite exposed end. Jap J Magn Reson Med. 2020;40(Suppl). (in Japanese)

59. Feynman RP, Leighton RB, Sands M. The Feynman lectures on physics Section 6–11. Pasadena:California Institute of Technology; 1966. http://www.feynmanlectures.caltech.edu. (Accessed: December 11, 2021)

60. Yamazaki M, Ideta T, Kudo S, Nakazawa M. Evaluation of artificial hip joint with radiofrequency heating issues during MRI examination: A comparison between 1.5 T and 3 T. Nihon Hoshasen Gijutsu Gakkai Zasshi 2016; 72:480–488. (in Japanese)

61. Kuroda K, Sunohara S, Yatsushiro S, et al., editors. Imagiing conditions and image quality for patients with MR-conditional implantable mediical devices: Norrmal volunteer study. Proceeding of 27th Annual Meeting of ISMRM, Paris, 2018; 643.

62. Faulkner W. B1+rms as a condition of use 2016. https://www.ismrm.org/smrt/E-Signals/2016FEBRUARY/eSig_5_1_hot_2.htm. (Accessed: December 11, 2021)

63. Baker KB, Tkach JA, Nyenhuis JA, et al. Evaluation of specific absorption rate as a dosimeter of MRI-related implant heating. J Magn Reson Imaging 2004; 20:315–320.

64. American Society for Testing and Materials (ASTM) International. F2182-19. Standard test method for measurement of radio frequency induced heating near passive implants during magnetic resonance imaging. West Conshohocken:ASTM, 2009.

65. National Electrical Manufacturers Association (NEMA). NEMA MS 8-2008. Characterization of the specific absorption rate for magnetic resonance imaging systems. standards publication. Arlington:NEMA, 2008.

66. American Society for Testing and Materials (ASTM) International. F2182-11a. Standard test method for measurement of radio frequency induced heating near passive implants during magnetic resonance imaging. West Conshohocken:ASTM, 2011.

67. National Electrical Manufacturers Association (NEMA). NEMA MS 8-2016. Characterization of the specific absorption rate for magnetic resonance imaging systems. standards publication. Arlington:NEMA, 2016.

68. Kokuryo D, Kumamoto E, Kuroda K. Recent technological advancements in thermometry. Adv Drug Deliv Rev 2020; 163–164:19–39.

69. Kuroda K. MR techniques for guiding high-intensity focused ultrasound (HIFU) treatments. J Magn Reson Imaging 2018; 47:316–331.

70. Ishihara Y, Calderon A, Watanabe H, et al. A precise and fast temperature mapping using water proton chemical shift. Magn Reson Med 1995; 34:814–823.

71. Kuroda K. Non-invasive MR thermography using water proton chemical shift. Int J Hyperthermia 2005; 21:547–560.

72. Rieke V, Butts Pauly K. MR thermometry. J Magn Reson Imaging 2008; 27:376–390.

73. Kuroda K. Temperature monitoring using chemical shift. In: Bottomley PA, Griffiths JR, eds. Handbook of magnetic resonance spectroscopy in vivo: MRS theory, practice and applications. Chichester:John Wiley & Sons; 2016; 401–414.

74. Weber H, Taviani V, Yoon D, Ghanouni P, Pauly KB, Hargreaves BA. MR thermometry near metallic devices using multispectral imaging. Magn Reson Med 2017; 77:1162–1169.

75. Detti V, Grenier D, Perrin E, Beuf O. Assessment of radiofrequency self-heating around a metallic wire with MR T1-based thermometry. Magn Reson Med 2011; 66:448–455.

76. Pfeil A, Drobnik S, Rzanny R, et al. Compatibility of temporary pacemaker myocardial pacing leads with magnetic resonance imaging: an ex vivo tissue study. Int J Cardiovasc Imaging 2012; 28:317–326.

77. Gensler D, Fidler F, Ehses P, et al. MR safety: fast T(1) thermometry of the RF-induced heating of medical devices. Magn Reson Med 2012; 68:1593–1599.

78. Weber H, Ghanouni P, Pascal-Tenorio A, Pauly KB, Hargreaves BA. MRI monitoring of focused ultrasound sonications near metallic hardware. Magn Reson Med 2018; 80:259–271.

79. Griffin GH, Ramanan V, Barry J, Wright GA. Toward in vivo quantification of induced RF currents on long thin conductors. Magn Reson Med 2018; 80:1922–1934.

80. Delcey M, Bour P, Ozenne V, Ben Hassen W, Quesson B. A fast MR-thermometry method for quantitative assessment of temperature increase near an implanted wire. PLoS One 2021; 16:e0250636.

81. Sapareto SA, Dewey WC. Thermal dose determination in cancer therapy. Int J Radiat Oncol Biol Phys 1984; 10:787–800.

82. van Rhoon G, Samaras T, Yarmolenko P, Dewhirst M, Neufeld E, Kuster N. CEM43°C thermal dose thresholds: a potential guide for magnetic resonance radiofrequency exposure levels? Eur Radiol 2013; 23:2215–2227.

83. International Electrotechnical Commission (IEC). IEC 60601-2-33:2010/COR2:2016. Corrigendum 2 - Medical electrical equipment - Part 2-33: Particular requirements for the basic safety and essential performance of magnetic resonance equipment for medical diagnosis. Geneva:IEC, 2016. https://webstore.iec.ch/publication/24208#additionalinfo. (Accessed: December 11, 2021)

84. National Electrical Manufacturers Association (NEMA). NEMA MS 14-2019. Characterization of radiofrequency (RF) coil heating in magnetic resonance imaging systems. standards publication. Arlington:NEMA, 2019.

85. Levine GN, Gomes AS, Arai AE, et al. Safety of magnetic resonance imaging in patients with cardiovascular devices: an American Heart Association scientific statement from the Committee on Diagnostic and Interventional Cardiac Catheterization, Council on Clinical Cardiology, and the Council on Cardiovascular Radiology and Intervention: endorsed by the American College of Cardiology Foundation, the North American Society for Cardiac Imaging, and the Society for Cardiovascular Magnetic Resonance. Circulation 2007; 116:2878–2891.

86. Baikoussis NG, Apostolakis E, Papakonstantinou NA, Sarantitis I, Dougenis D. Safety of magnetic resonance imaging in patients with implanted cardiac prostheses and metallic cardiovascular electronic devices. Ann Thorac Surg 2011; 91:2006–2011.

87. Dandamudi S, Collins JD, Carr JC, et al. The Safety of cardiac and thoracic magnetic resonance imaging in patients with cardiac implantable electronic devices. Acad Radiol 2016; 23:1498–1505.

88. Ono M, Suzuki M, Isobe M. Feasibility, safety, and potential demand of emergent brain magnetic resonance imaging of patients with cardiac implantable electronic devices. J Arrhythm 2017; 33:455–458.

89. Strom JB, Whelan JB, Shen C, Zheng SQ, Mortele KJ, Kramer DB. Safety and utility of magnetic resonance imaging in patients with cardiac implantable electronic devices. Heart Rhythm 2017; 14:1138–1144.

90. Schukro C, Puchner SB. Safety and efficiency of low-field magnetic resonance imaging in patients with cardiac rhythm management devices. Eur J Radiol 2019; 118:96–100.

91. Bhuva AN, Moralee R, Brunker T, Lascelles K, Cash L, Patel KP, et al. Evidence to support magnetic resonance conditional labelling of all pacemaker and defibrillator leads in patients with cardiac implantable electronic devices. Eur Heart J 2021;ehab350.

92. Glikson M, Nielsen JC, Kronborg MB, et al. 2021 ESC guidelines on cardiac pacing and cardiac resynchronization therapy. Eur Heart J 2021; 42:3427–3520.

93. Glikson M, Nielsen JC, Kronborg MB, et al. ESC guidelines on cardiac pacing and cardiac resynchronization therapy. Eur Heart J 2021; 42:3427-3520.

94. International Standard Organization (ISO). ISO 5841-3:2013. Implants for surgery — Cardiac pacemakers — Part 3: Low-profile connectors (IS-1) for implantable pacemakers. Geneva: ISO; 2012.

95. Do DH, Eyvazian V, Bayoneta AJ, et al. Cardiac magnetic resonance imaging using wideband sequences in patients with nonconditional cardiac implanted electronic devices. Heart Rhythm 2018; 15:218–225.

96. Indik JH, Gimbel JR, Abe H, et al. 2017 HRS expert consensus statement on magnetic resonance imaging and radiation exposure in patients with cardiovascular implantable electronic devices. Heart Rhythm 2017; 14: e97–e153.

97. Nazarian S, Hansford R, Rahsepar AA, et al. Safety of magnetic resonance imaging in patients with cardiac devices. N Engl J Med 2017; 377:2555–2564.

98. Russo RJ, Costa HS, Silva PD, et al. Assessing the risks associated with MRI in patients with a pacemaker or defibrillator. N Engl J Med 2017; 376:755–764.

99. Seewöster T, Lobe S, Hilbert S, et al. Cardiovascular magnetic resonance imaging in patients with cardiac implantable electronic devices: best practice and real-world experience. Europace 2019; 21:1220–1228.

100. Shulman RM, Hunt B. Cardiac implanted electronic devices and MRI safety in 2018-the state of play. Eur Radiol 2018; 28:4062–4065.

101. Meyers J, Prutchi D, Shehada R. Input impedance comparison of MR-conditional cardiac implantable pulse generators at the 1.5T MR frequency of 63.87 MHz. Proceeding of the 2021 Annual Meeting of ISMRM & SMRT, Online, 2021; 2311.

102. Prutchi D, Meyers J, Shehada R. RF Impedance of MR-conditional pacemaker leads when connected to implantable pulse generators from different MR-conditional systems. Proceeding of the 2021 Annual Meeting of ISMRM & SMRT, Online, 2021; 2281.

103. Prutchi D, Meyers J, Shehada R. Importance of pacemaker lead preconditioning for MR safety in-vitro studies. Proceeding of the 2021 Annual Meeting of ISMRM & SMRT, Online, 2021; 2282.